This is a preprint, the final version is subject to change, of the American Mineralogist (MSA)
Cite as Authors (Year) Title. American Mineralogist, in press.
(DOI will not work until issue is live.) DOI: http://dx.doi.org/10.2138/am.2013.4448

Revision 2

Medium-range order in disordered K-feldspars by multinuclear NMR

Luis Sánchez-Muñoz[1*], Jesús Sanz[2], Isabel Sobrados[2], and Zhehong Gan[3]

[1]Instituto de Cerámica y Vidrio (CSIC) Kelsen 5, 28049 Madrid, Spain

[2]Instituto Ciencia de Materiales de Madrid (CSIC), 28049 Madrid, Spain

[3]National High Magnetic Field Laboratory, Florida State University, Tallahassee, FL 32310, USA

(*Corresponding author: lsm@icv.csic.es)

ABSTRACT

The structures of K-rich feldspar (K>Na)$AlSi_3O_8$ are currently described as "ideal" crystals with periodic average structures from Bragg diffraction maxima obtained by reciprocal-space techniques. Polymorphism is explained by variable substitutional disorder of framework Si and Al cations in tetrahedral T sites, and positional disorder of cavity alkali cations in a single M site. Here, high-resolution magic-angle spinning multi-nuclear magnetic resonance spectroscopy, leading to ^{29}Si, ^{27}Al and ^{23}Na spectra at 9.4 as well as ^{27}Al, ^{39}K and ^{23}Na spectra at 19.6 T, has been used to investigate the "real" structures along the order-disorder series of K-feldspar crystals. The "ideal" and "real" structure coincides only in the perfectly long-range ordered triclinic end-member of the low microcline structure. Long-range disordered structures (either with monoclinic or triclinic symmetry by X-ray diffraction) show non-random disorder at the medium-range scale, triclinic-like distortions with four sets of T sites for framework atoms, two sets of M sites for alkali atoms, and Al-O-(K,Na) multi-site correlations by NMR spectroscopy. The K-feldspar structures can be described by a medium-range structure using the number of Al atoms per four-membered rings of tetrahedra, with "…-2-0-2-0-…" chains for microcline and orthoclase where the Al-occupancies $t_1O > t_2m > t_2O \approx t_1m$, and with "…-1-1-1-1-…" chains for valencianite

and sanidine, in which $t_1O > t_2m \approx t_2O \approx t_1m$. Framework cations respect Loewenstein's rule (Al-O-Al avoidance), as well as some additional constraints of charge dispersion involving deficiency of Si atoms in Q^4 (4Si,0Al), (1Si,3Al) and (0Si,4Al) environments, which are particularly strong in valencianite. These "real" structure features cannot be described by "ideal" structures owing to the lack of resolving power of the reciprocal-space techniques.

KEYWORDS: K-feldspars, NMR, medium-range order, valencianite, order-disorder series

INTRODUCTION

Taylor's model of the archetypal structure of feldspars, induced from X-ray diffraction (XRD) data of *sanidine* (Taylor 1933, Taylor et al. 1934), suggests a monoclinic *C*2/m average symmetry if the framework of tetrahedra is idealized in a topology where the actual occupancy of T sites by Si and Al atoms is disregarded. The structure consists of three-dimensionally linked SiO_4 and AlO_4 tetrahedral units with two crystallographically non-equivalent tetrahedral sites, T_1 and T_2. The T sites form double crankshaft chains of four-member rings, replicated by mirrors parallel to (010). The alkali cations, located at a single M site inside an irregular cavity, ensure local electrostatic (ionic) neutrality. Immediately thereafter, Barth (1934) proposed an order-disorder relationship in the Si, Al distribution of the T sites to explain the structural diversity of K-feldspar in Nature. Subsequent structural refinements (see Taylor 1965, for an early review) confirmed this hypothesis when site occupancies are correlated with mean T-O distances. As Si and Al atoms have similar X-ray scattering factors, it is impossible to refine site occupancies using X-ray data (Smith 1954). Sanidine was

regarded as the high-temperature phase having completely random disorder, whereas *orthoclase* is seen to be partially ordered, with preferential segregation of Al atoms into the T_1 sites. Further Si/Al ordering can produce *microcline*, the low-temperature phase, with a lowering of the symmetry from *C*2/m to *C*-1, and a distortion of the unit-cell shape. The four T sites are labeled T_1O, T_1m, T_2O and T_2m, with the Al atoms concentrated in the T_1O site and Si occupying three other sites (Megaw 1956). The Al-occupancies Al/(Al+Si) of the T sites, denoted as t_1O, t_1m, t_2O and t_2m, allows the distinction between low microcline where $t_1O = 1.0$ and $t_1m = t_2O = t_2m = 0.0$ and intermediate microcline where $t_1O > t_1m > t_2O = t_2m$ (Ribbe 1983). It has been suggested that in the K-feldspars alkali atoms may have positional disorder along the order-disorder series, occupying slightly different positions around a single M site (see discussions by Megaw 1959 and Ribbe 1994, p. 21-24).

The description of crystal structures of K-feldspar in terms of time and space averages derived from Bragg diffractions in reciprocal-space techniques as "ideal" crystal structures, and the calculation of the degree of Si/Al order from T-O distances, have some weaknesses. That approach ignores the omnipresent X-ray diffuse scattering (Laves 1950) arising from structural modulations in orthoclase (McConnell 1965) and from intrinsic distortions of the framework due to different sizes of the AlO_4 and SiO_4 tetrahedra in sanidine (Pleger 1996). Random disorder in sanidine has not been demonstrated from average T-O distances induced by more recent determinations by XRD (Scambos et al. 1987; Kimata et al. 1996b) or neutron diffraction determinations (Brown et al. 1974). The lattice model for orthoclase with an average monoclinic symmetry is inconsistent with the local triclinic structure detected by other techniques (McLaren and Fitz Gerald 1987; Sánchez-Muñoz et al. 1998), as first indicated by

Laves and Goldsmith (1961). In addition, it is impossible to determine the exact Al occupancy of disordered Na-feldspars only on the basis of T-O bond distances, as the T sites have intrinsically different T-O bond lengths (Winter et al. 1979). This finding calls into question the usefulness of the approach in this family of minerals. The effect of alkali atoms (as only one M site is invoked), as well as possible strain effects (Eggleton and Buseck 1980) and the importance of the size of domains or twins to produce coherent diffraction (Ribbe 1983), also must be considered.

Available nuclear magnetic resonance (NMR) data for K-feldspars (Laves and Hafner 1962; Lippmaa et al. 1980; Smith et al. 1984; Kirkpatrick et al. 1985; Sherriff and Hartman 1985; Phillips et al. 1988; Zhou et al. 1994 and 2001; Xiao et al. 1995; Sánchez-Muñoz et al. 1998 and 2006a; Anbalagan et al. 2009) have supported the Si/Al order-disorder hypothesis partially. In particular, the NMR parameters of monoclinic K-feldspars do not correlate well with site occupancies determined by XRD (Xiao et al. 1995). Most of the available NMR studies have been performed at low fields using rather few samples, with limited characterization. The more disordered states have been investigated in much less detail than the ordered counterparts, owing to lack of sufficient spectral resolution. Data from the ^{29}Si and ^{27}Al spectra have not been correlated with those from the ^{39}K and ^{23}Na spectra along the order-disorder series. Moreover, disordered states having a triclinic symmetry (Chaison 1950; Laves 1950), termed *valencianite* by Akizuki and Sunagawa (1978), have been disregarded in most NMR investigations. In addition, ^{39}K spectra are difficult to obtain because of the low sensitivity and large quadrupolar coupling associated with highly asymmetric sites, particularly in disordered structures.

In this paper we address the above questions by means of multinuclear NMR analysis at 9.4 and 19.6 T using specimens very similar to those characterized by X-ray methods in the literature to build up the conventional order-disorder model. The "real" structures are investigated to evaluate the hypotheses that: 1) the Si, Al occupancies in the framework T sites cannot be investigated independently of the distribution of alkali cation in the M split-sites in the cavity, 2) a quasi-triclinic local symmetry exists along the order-disorder series, and 3) the type of K-feldspar can be described with a specific polyatomic arrangement at the medium-range length scale, inaccessible with the resolving power of XRD techniques.

THE K-FELDSPARS

Table 1 indicates the chemical composition, provenance and host of the thirty three natural specimens and synthetic samples of feldspars used in this work, including selected K-feldspar specimens well known in literature, a sample with stoichiometric $KAlSi_3O_8$ composition from hydrothermal crystallization at high temperatures and high pressure (sample *7294*), and three samples from ion-exchanged experiments using previous natural specimens as starting materials to obtain K-feldspar with composition close to $KAlSi_3O_8$ in a range of order-disorder states (samples *K-ASGS*, *K-EU2* and *K-713r**). A crystal of Na-feldspar (specimen *CLBR*) was included. Most specimens are gem-quality materials in terms of transparency and uniformity at the optical scale, and display a single structural state in their XRD patterns. The terms used in this work include the recommendations of the International Mineralogical Association (IMA) to designate mineral species (Barth 1934), including microcline (MI), orthoclase (OR) and sanidine (SA). However, the term "valencianite" (VA) is needed to refer to some K-

126 feldspar samples that cannot be labelled with the previous names; see Smith (1974) for
127 an extended review of nomenclature.
128
129 **Microcline**
130 Specimen *11924* is close to that used by Blasi et al. (1984a) for the structure
131 determination of the low microcline end-member. Specimen *9544* has a XRD pattern
132 very close to that of low microcline but shows regular Albite-Pericline twinning at both
133 the optical and transmission electron microscopy (TEM) scales (Sánchez-Muñoz et al.
134 2012). Specimens *176* and *116* show heterogeneous optical extinction and "irregular
135 twinning" (as described by Bambauer et al. 1989) at the TEM scale (Sánchez-Muñoz et
136 al. 2006a). They correspond to the intermediate microcline XRD variety of Ribbe
137 (1983). Specimen *FB4* shows a heterogeneous diffraction pattern with broad (*hkl*), (*hk*0)
138 and (0*kl*) peaks, indicating a triclinic structure with low obliquity.
139
140 **Orthoclase**
141 Orthoclase can form from high-temperature precursor like sanidine (normally
142 with a high content of Na in solid solution), or at much lower temperatures in
143 hydrothermal veins as crystals of adularia (with lower Na contents in solid solution).
144 Because exsolution of the original feldspars takes place simultaneously with local
145 ordering during slow cooling, a low Na content reduces the contribution of Na-feldspar
146 impurities to the K-feldspar spectra, improving the experimental resolution. Thus,
147 crystals of adularia were selected instead of plutonic or metamorphic grains. The typical
148 "tweed" pattern in our specimens (Table 1) and the associated orthogonal diffuse streaks
149 in the [001] zone axis of selected-area electron diffraction (SAED) patterns, were
150 studied by TEM by Sánchez-Muñoz et al. (1998), including the specimen *ASGS* from

Saint Gotthard, Switzerland, similar to that originally studied by McConnell (1965), in which the tweed pattern was first noted. Our orthoclase specimens have a higher Na content in solid solution than the valencianite specimens, and negligible content of the anorthite component.

Valencianite

Specimens of valencianite are defined by the characteristics described in Chaison (1950), Laves (1950) and Akizuki and Sunagawa (1978): triclinic symmetry with low obliquity on the basis of optical and diffractometric data, very low Na content in solid solution (Table 1), and the lack of tweed or twin microstructures at the TEM scale, as well as absence of diffuse streaks in SAED patterns. This variant indicates a particularly low temperature of crystallization, and thus, the triclinic character must be formed during crystallization at a temperature lower than the monoclinic-triclinic transition. In contrast, microcline almost invariably shows some residual twinning from the phase transformation of a monoclinic high-temperature precursor. Specimen *AGM*, from "Valenciana mine" in Guanajuato, Mexico, is very uniform and has the highest obliquity ($\gamma = 89.74^{\circ}$) of our specimens. Specimen *1407* can be considered valencianite on the basis of chemical and microstructural features (as well as from the NMR data), but no peak splitting in (*hkl*), (*hk*0) and (0*kl*) reflexions was detected. This specimen is therefore similar to adularia from Hishikari, Japan (Zhou et al. 2001).

Sanidine

The specimens used in this work are single crystals separated from glass material of felsic volcanic rocks, except specimen *RABB*, from a subvolcanic granitic pegmatite (O'Brient 1986, Keefer and Brown 1978). Specimens *RABB* and *SBKS* have

well developed submicroscopic albite films from partial exsolution. The other specimens of sanidine do not show any evidence of exsolution. Additional features of specimen *EU2* can be found in Sánchez-Muñoz et al. (2007). Specimens *SVNI-1* and *SVNI-2* are analogous to the one used by W.H. Taylor in 1933 in the first X-ray determination of the structure of sanidine. Specimen *713r* is also comparable to that used in some other crystal-structure determinations (Brown et al. 1974; Kimata et al. 1996a and 1996b).

Synthetic samples

Ion-exchange experiments were conducted with orthoclase *ASGS* and sanidine *EU2* to obtain samples with pure $KAlSi_3O_8$ composition as *K-ASGS* and *K-EU2*. Because valencianite invariably has a low content of Na in solid solution, no ion-exchange experiments were done in this case. Fine powders of the selected specimens were mixed with molten KBr at 825°C for 30 hours. In addition, the same experiments were performed at higher temperatures for specimen *713r* to obtain sample *K-713r** at 1050 ºC for 15 hours. In all cases, the ion-exchange products showed XRD pattern compatible with a monoclinic structure, as the original material had, i.e. no departure in the monoclinic symmetry was detected by XRD because of ion-exchange experiments. Sample *7294* was synthesized at 725 ºC and 3 kbars for 168 h from a H_2O-oversaturated melt of $KAlSi_3O_8$ composition and with KF and AlF_3 additions as mineralizers, in the Institute des Sciences de la Terre d'Orléans (CNRS, France), with the help of Prof. François Delbove.

EXPERIMENTAL METHODS

Chemical analysis

Spatially resolved quantitative chemical analysis of the major elements Si, Al, Na, K and Ca were performed by electron microprobe analysis (EMPA). We carried out an average of five or six analyses per sample, using a point-counting technique to obtain information on the chemical homogeneity, in a SX-50 instrument by Mr. Olivier Rouer in Institute des Sciences de la Terre d'Orléans (ISTO) in CNRS (France). Natural K-rich and Na-feldspars as well as synthetic pure K- and Na-feldspars (also synthesized at ISTO) were used as chemical standards, which were previously analyzed by the electron probe in several experimental conditions to get the maximum signal and minimum loss of Na. The spot diameter of the probe was circa 1 μm. The final operating conditions were 15 kV and 25 nA. A ZAF software was used for the correction of the matrix effects. The chemical compositions was expressed as $Or_xAb_yAn_z$ (x+y+z = 100) (Table 1), with Or, Ab and An expressing the molar content of $KAlSi_3O_8$, $NaAlSi_3O_8$ and $CaAl_2Si_2O_8$ components in solid solution. Only some specimens of sanidine show an appreciable Ca content.

Nuclear Magnetic Resonance.

High-resolution ^{29}Si, ^{27}Al and ^{23}Na magic angle spinning (MAS) NMR spectra were recorded at 79.49, 104.23 and 105.80 MHz (9.4 T magnetic field), by spinning the sample at the magic angle (54°44") using a Bruker Avance 400 spectrometer equipped with a Fourier transform unit of the Instituto de Ciencia de Materiales de Madrid (CSIC) in Spain. The samples were spun in the range of 4000 to 20000 Hz. The pulse lengths are 4, 2, and 2 μs; the recycle delays are 1800, 5 and 5 s; and the *rf* field are 60, 50, 50 kHz, respectively for the ^{29}Si, ^{27}Al and ^{23}Na nuclei, to get a maximum in the

intensity of the experimental signal. Recycle-delay times for ^{29}Si spectra were tested for values between 60 and 1800 seconds in samples with different structural state and chemical compositions to avoid saturation effects in the ^{29}Si signals. Crystals from volcanic rocks show iron impurities in T sites at the ppm scale, and a recycle time of 60 seconds was sufficient to obtain the ^{29}Si spectra. However, crystals formed at low temperatures do not show such paramagnetic impurities, and the best results were obtained for 1800 second relaxation delays. Therefore, in order to get appropriate comparison of the NMR spectra of the whole set of specimens and samples, 1800 seconds were used in all cases. The number of accumulations was 200 for Al, and 50 for Si and Na signals.

High-resolution ^{27}Al, ^{39}K and ^{23}Na spectra magic angle spinning (MAS) NMR spectra were acquired also at 216.14, 38.89 and 219.42 MHz (19.6 T magnetic field), using an 830 MHz Bruker DRX NMR spectrometer at the National High Magnetic Field Laboratory (NHMFL) in Tallahassee, Florida, USA. Spectra were recorded with a 4 mm home-built MAS probe at 10 kHz sample spinning. The pulse lengths are 0.75, 2, 0.75 μs; the recycle delays are 2, 1, 2 s; and the *rf* field are 70, 50, 70 kHz, respectively for the ^{27}Al, ^{31}K and ^{23}Na nuclei. The number of accumulations was 128 for ^{27}Al, and 1024 for ^{23}Na signals, and between 3712 scans (e.g. in specimen *116*) and 65536 scans (e.g. in specimen *11924*) for ^{39}K.

Chemical shifts are reported in ppm relative to external references at room temperature, specifically, to tetramethylsilane (TMS) for ^{29}Si, 1 *M* AlCl3 aqueous solution for ^{27}Al, KBr for ^{39}K and 1 M NaCl aqueous solution for ^{23}Na spectra. The mean error in the measured chemical shift of the NMR components was approximately

1 ppm for ^{29}Si, ^{27}Al and ^{23}Na spectra, and circa 10 ppm for ^{39}K spectra. Kaolinite, KBr and Na_2HPO_4 were used as samples to calibrate the pulse widths for ^{27}Al, ^{39}K and ^{23}Na, respectively.

The ^{29}Si signals (I = 1/2) were analyzed by comparison of experimental curves with simulated profiles using Gaussian components for the different crystallographic sites in distinct crystallochemical environments, with identical linewidths, and variable intensities related to the Si, Al occupancies of the T sites. There is no physical basis for assigning identical linewidths to geometrically different sites in distinct chemical environments in the simulation of a single spectrum. However, we limited the number of fit parameters to a minimum, mainly chemical shifts and relative areas (or intensities) in the deconvolution of spectra. Additional difficulties come from the lack of information about chemical shifts for the Al $\leftrightarrow$ Si substitutions in the second-coordination sphere, as well as the effect of K and Na atoms. Finally we chose 4.85 ppm as a shift between Si(nAl) and Si([n+1]Al) peaks for all the simulations, a value compatible with other NMR studies of aluminosilicates with tectosilicate structures (e.g., Klinowski et al. 1982; Phillips and Kirkpatrick 1995; Xiao et al. 1995); its use allows the reproduction of the main spectral features of most K-feldspars.

The ^{27}Al, ^{39}K and ^{23}Na NMR spectra were fitted with Bruker WINFIT and DM2011 (Massiot et al. 2002) software, to calculate the quadrupolar constants C_Q, the asymmetry factor η and the linewidth of each component. Where the second-order quadrupolar effects are visible in the central transition, the chemical shift and the quadrupolar constant were determined from the fitting of the central transition profile. An estimation of the second-order quadrupolar correction to the chemical shift was

obtained from the displacement of the center of gravity with external magnetic field from 9.4 to 19.6 T, using the SORGE diagram of Massiot et al. (1995). Where a single magnetic field was used and the second-order quadrupolar effects are not visible, the values of chemical shift cannot be determined.

X-ray diffraction patterns

The feldspars were studied by powder XRD patterns to identify the mineral species and varieties using an INEL CPS 120 instrument with Co $K\alpha_1$ radiation at 30 kV and 25 mA, with Si as an internal standard. Spectra were recorded at 0.3º /min with 2º slits on samples placed in turning glass capillary tubes with a diameter of 0.50 mm. With these patterns, the K-feldspars were identified (last column in Table 1) using XRD data from Blasi (1984), Blasi et al. (1984b) and Kroll et al. (1986).

Eleven specimens and samples of K-feldspars, belonging to one of the four types listed in Table 1, were selected to obtain unit-cell parameters using Rietveld refinement by means of the whole-pattern decomposition or profile-matching method (Table 2). The procedure is known as the LeBail fitting (LeBail et al. 1988, Rodriguez-Carvajal 1993), using the FULLPROF (Rodríguez-Carvajal 2001) and the WinPLOTR software (Roisnel and Rodriguez-Carvajal 2001). This method does not require any structural information except approximate unit-cell dimensions and resolution parameters. These particular patterns were obtained using a Philips PANalytical X'Pert PRO MPD Alfa1 diffractometer. Incident X-ray radiation was produced with a PW 3373/10 Cu LFF DK175180 instrument, with Cu $K\alpha_1$ radiation at 45 kV and 40 mA. XRD patterns were recorded between 4.0 and 130.0 º2θ, with a step size of 0.008º in a continuous scan mode, using a Ge monochromator (Inc Beam 1xGe111 Cu/Co), a X'Celerator RTMS-

type detector, and a X'Pert program for data collection. Cell parameters were used to obtain order parameters, specifically Σt_1 ($t_1O + t_1m$) and Σt_2 ($t_2O + t_2m$) using formulas of Kroll and Ribbe (1987), to classify the K-feldspar specimens and samples as XRD varieties (Ribbe 1983). With this study, the IMA-approved mineral species (Table 1) were correlated with the XRD varieties (Table 2), except for "valencianite" specimens, in which the triclinic character derived from cell angles is not correlated with order-disorder based on unit-cell dimensions (see Smith 1974, for additional discussion about K-feldspar nomenclature). Hence, as a whole, these materials do not correlate well with the paradigmatic sequence of K-feldspar formation on cooling, in the sequence sanidine $\rightarrow$ orthoclase $\rightarrow$ microcline. In particular, specimen AGM has the sharpest peak splitting from obvious triclinic character and shows the most disordered structure on the basis of cell dimensions, with the lowest Σt_1 value (Table 2). On the other hand, specimen *1407*, with a relatively high Σt_1 value, shows no evidence of the splitting of peaks as expected from a sharp monoclinic lattice.

RESULTS AND SPECTRAL SIMULATIONS

^{29}Si MAS NMR spectra

In Figures 1 to 4, we summarize representative ^{29}Si spectra of the K-feldspar samples studied. Tables 3 and 4 (and Table 5 and 6 in supporting information online) show the peak positions and intensities used in the spectral simulations of alternative models. In all cases, the specific intensities of peaks for each T site with the variable chemical environment were calculated assuming a fixed Si:Al ratio equal to 3:1 and Al-O-Al avoidance (Loewenstein's rule: Loewenstein 1954), using the expressions of Xiao et al. (1995), but in the following tetrahedral environments: the T_1O site is surrounded by 1 T_1m, 1 T_1O and 2 T_2m sites; the T_1m by 1 T_1O, 1 T_2m and 2 T_2O; the T_2O by 1

326 T_1O, 1 T_2m and 2 T_1m; and finally the T_2m by 1 T_1m, 1 T_2O and 2 T_2O. The chemical
327 shift difference between the peaks for Si(nAl) and Si(n+1Al) environments was
328 assumed to be +4.85 ppm in all cases. The relationship between the peak intensity I_x in
329 % and the Al occupancy t_x is given by $t_x = 1 - 3(I_x/100)$. With these basic assumptions,
330 the main spectral features of most K-feldspars can be reasonably explained.
331
332 Two contrasting types of ^{29}Si spectra were observed. Microcline, orthoclase,
333 valencianite and sanidine (when it is close to the $KAlSi_3O_8$ composition, either from
334 K→Na ion-exchange of natural Na-rich sanidine or by stoichiometric crystallization in
335 hydrothermal experiments) have spectra with three maxima at -95.0 ± 0.3, -97.6 ± 0.3
336 and -100.8 ± 0.5 ppm, and some additional lateral shoulders (Figs. 1, 2 and 3).
337 However, natural sanidine (Fig. 4) consist of two maxima at -96.5 ± 0.5 and -100.2 ±
338 0.4 ppm with some minor lateral shoulders in non-exsolved specimens (e.g. specimen
339 *EU2*), whereas two maxima at -97.5 ± 0.3 and -100.5 ± 0.3 ppm with a well developed
340 shoulder at ~-95.2 ppm, are found in specimens in which an exsolution-induced
341 microtexture is developed (e.g. specimen *RABB*).
342
343 Figure 1 displays the ^{29}Si spectra of microcline specimens. The spectrum of
344 specimen *9544* consist of three Gaussian peaks of equal intensity and width, attributed
345 to Si atoms in T_2m (2Si,2Al) at -95.2 ppm, T_2O (3Si,1Al) at -97.2 ppm, and T_1m
346 (3Si,1Al) at -100.9 ppm. This spectrum is consistent with the low microcline structure
347 as the fully ordered end-member of the order-disorder series, with Al atoms occupying
348 only the T_1O site (Lippmaa et al. 1980, Smith et al. 1984; Kirkpatrick et al. 1985;
349 Phillips et al. 1988; Xiao et al. 1995). If partial disorder exists, new signals from Si at
350 T_1O and new chemical environments are generated as shown in three specimens of

intermediate microcline (Figs. 1b to 1d). These spectra were reasonably simulated with chemical shifts similar to those of the low microcline, and the signal from Si atoms in T_1O (3Si,1Al) at -102.2 ppm. This analysis suggests that Al atoms are mainly located at T_1O sites, with $t_1O > 0.73$ as expected from XRD data, but complemented with $t_2m > t_2O \approx t_1m$ values (Table 3), in contrast to conventional models from XRD data where $t_1m > t_2O \approx t_2m$ occupancies are indicated.

Surprisingly, orthoclase specimens have very similar spectra in all cases (Fig. 2a), consisting of three peaks with maxima at almost the same positions of microcline, and with analogous intensity (but the peak at -100.8 ppm has larger area than the other two peaks), as well as some minor lateral shoulders at -92.5 and -105.2 ppm. The ion-exchange experiments do not change the ^{29}Si spectra of orthoclase significantly (compare *ASGS* with *K-ASGS* in Fig. 2a). No indication of obliquity was found in the XRD pattern of sample *K-ASGS* after the ion-exchange experiments, as it was absent before the cation exchange. The spectral simulations compatible with the experimentally observed spectra of orthoclase (Fig. 2b) were obtained by considering the t_1O value to be between 0.70 and 0.80, a t_2m value between 0.10 and 0.20, t_2O and t_1m values between 0.05 and 0.10, and δT_1O (3Si,1Al) = -101.7 ppm, δT_2m (2Si,2Al) = -94.9 ppm (Table 3, and Table 5 in supporting information online). Our simulation of the orthoclase spectra shows that $t_2m > t_2O \approx t_1m$ is very characteristic of this structure. However, the signal from Si at T_1m (4Si,0Al) is invariably more developed in the simulations that in the original spectra, indicating that additional restrictions to that of the Loewenstein's rule must be at work, for instance some additional dispersion of charges reducing the development of (4Si,0Al) environment at the T_1m site (* in Fig. 2). The ^{29}Si spectrum for a two-step monoclinic orthoclase was simulated in Figure 2c with

a typical Si, Al distribution over two T sites with $t_1O = t_1m = 0.4$ and $t_2O = t_2m = 0.1$ (Table 6 in supporting information online), as generally suggested by XRD. In addition, the spectral simulation of the one-step triclinic orthoclase with $t_1O = 0.7$ and $t_1m = t_2O = t_2m = 0.1$ (Table 6 in supporting information online) is shown in Fig. 2d. Both alternative models reproduce the experimental results more poorly than the simulations already suggested in Figure 2b, particularly if a monoclinic structure is considered.

Figure 3 exhibits the ^{29}Si spectra of the valencianite specimens, which are characterized mainly by the same three peaks of previous feldspars, however the peak at -100.7 ppm is broader and more inhomogeneous having almost double area and higher intensity than the other two peaks at -95.2 and -97.5 ppm, displaying also minor lateral signals at -90.1, -92.5 and -105.2 ppm. The spectra of the less disordered valencianite specimens can be simulated partially with t_1O values of about 0.6 and $t_2O > t_2m \approx t_1m$ (specimens *1406* and *1109*: Fig. 3a, Table 3). The broad peak with a maximum at about -105.2 ppm, formed by the addition of signals from Si at T_1O (4Si,0Al), T_1m (4Si,0Al) and T_2m (4Si,0Al), and that at -90.1 ppm, reflecting Si at T_2O and T_2m with a (1Si,3Al) environment (asterisk in Fig. 3), are much more developed in the simulations than in the experimental spectra. The more disordered valencianite specimens, as judged from NMR results (specimens *AGM* and *1407*), are shown in comparison with two simulated spectra for $t_1O = 0.4$ and $t_1m = t_2O = t_2m = 0.2$ (sim1 and sim2) in Figure 3b. The spectrum sim1 is constructed with all the possible Si Q^4 (nAl) environments for Si:Al = 3:1 and peak intensities complying Loewenstein's rule. However, spectrum sim2 considers only the four major sites compatible with the same Al occupancy, i.e., T_1O (3Si,1Al), T_1m (3Si,1Al), T_2O (3Si,1Al) and T_2m (2Si,2Al), for which the peak positions are close to the standard values in microcline and orthoclase, and a wider

401 linewidth (see Table 3 for details). It is clear that the experimental spectra are
402 intermediate between these two cases, indicating that strong homogenization on the
403 charge distribution occurs throughout the framework during growth of these distinctive
404 disordered structures, at a low temperature.
405
406 Figure 4a shows the ^{29}Si NMR spectra of specimens *EU2* and *SVNI-2*; both are
407 very similar to the sample studied by Taylor (1933) in that they have a high sodium
408 content in solid solution (Table 1) as a consequence of a high temperature of
409 crystallization from alkali-rich magmas in a volcanic environment. Their spectra show
410 two maxima interpreted as corresponding to T_1 and T_2 sites in a monoclinic lattice
411 (Kirkpatrick et al. 1985, Zhou et al. 1994, Anbalagan et al. 2009), as expected from
412 Taylor's model. Where sanidine shows exsolution, the spectra have an additional
413 shoulder at -95.1 ppm, also resolved in specimens *RABB* and *SBKS*. However, samples
414 of synthetic K-feldspar of $KAlSi_3O_8$ composition, acquired either by hydrothermal
415 crystallization from a melt at high temperature (sample *7294*) or by K→Na ion-
416 exchange reactions at 800ºC (sample *K-EU2*) or at 1050ºC (sample *K-713r**), invariably
417 have three maxima, approximately at the same chemical shift as found in the other K-
418 feldspar types, as was also reported for an adularia crystal with a high sanidine XRD
419 pattern (Zhou et al. 2001). Note that if Na atoms are replaced with K atoms by ion
420 exchange at 800ºC, the Si, Al distribution is not disturbed, whereas some modifications
421 are expected in heating experiments performed at 1050ºC. No obliquity was detected in
422 the XRD patterns of the sanidine specimens after the ion-exchange experiments. Our
423 findings suggest the presence of more spectroscopically distinct or real-space sites than
424 are considered by the monoclinic lattice model. It follows that the single peak at -97.0
425 ppm in natural sanidine must be due to the coalescence of two Si signals, T_2O (3Si,1Al)

and T_2m (2Si,2Al), which is induced by the partial substitution of K atoms for the smaller Na atoms. The displacement effect is higher in the T_2m (2Si,2Al) signal, the one with a higher content of Al atoms in the second coordination sphere. The best simulations of the three-maximum sanidine spectra were obtained using: 1) the same line positions as in orthoclase and valencianite; 2) similar Si, Al occupancies as in valencianite (the t_1O value is considerably larger than the other three values); and 3) larger linewidths (Fig. 4b, Table 3). Shoulders at -92.5 and particularly at -105.5 ppm are well developed in the spectrum of K-substituted sanidine, but they are not as large as in the simulated spectra.

The spectra resulting from a structure with a fully disordered Si, Al distribution, where the four sites have the same Al occupancies (i.e., $t_x = 0.25$), were also simulated either with a monoclinic structure (Fig. 4c) or a local triclinic symmetry (Fig. 4d) for sake of comparison. In the first case, only two populations of T sites are considered, i.e., -97.8 – 4.8 = -93.0 ppm for T_2O (3Si,1Al) = T_2m (3Si,1Al), whereas in the second case, the spectrum is the sum of four identical populations with different chemical shifts (triclinic high sanidine in Table 6, in supporting information online). The two simulations are farther from the experimental spectra of any sanidine specimen than the proposed model in Figure 4b, where a large t_1O value in comparison with the other three site occupancies is assumed. A decrease in the shielding at ^{29}Si between 4.0 and 5.5 ppm arising from the substitution of Al for Si atoms in the second-sphere coordination did not reproduce a profile based on two maxima only. The ^{29}Si spectrum of sanidine based on two maxima was found only in Na-rich specimens, and it is particularly far from the model of random disorder in a monoclinic lattice (Fig. 4c).

451

452

453 **^{27}Al MAS NMR spectra**

454 Because Loewenstein's rule was so useful in the interpretation of the ^{29}Si spectra,
455 the Al atoms are expected to be systematically surrounded by four Si atoms, and the
456 interpretation of the spectra could be straightforward. On this basis, one should be able
457 to resolve signals arising from Al atoms surrounded by 4 Si at different structural sites,
458 having different average T-O distances, by this technique. However, the second-order
459 quadrupolar effect involves difficulties in the expected spectral resolution of the
460 different T sites, which can be partly improved by the use of a high external magnetic
461 field. Thus, ^{27}Al MAS NMR spectra were obtained and compared at 9.4 and 19.6 T
462 (Table 4).

463

464 Figure 5 shows the central transition (C.T.) ½→- ½ in the ^{27}Al MAS NMR spectra
465 at 9.4 T of Al atoms in tetrahedral coordination for the fully ordered end-member close
466 to the $KAlSi_3O_8$ composition with the low-microcline XRD pattern in specimen *11924*
467 (Fig. 5a), the $NAlSi_3O_8$ composition with low albite XRD pattern in specimen *CLBR*
468 (Fig. 5b), the disordered sanidine with stoichiometric $KAlSi_3O_8$ composition in sample
469 *7294* (Fig. 5c). The spectrum of low microcline shows a broad line due to second-order
470 quadrupolar effects (maxima 1 and 2 and shoulder 3), ascribed to a single crystalline
471 position of Al atoms in the T_1O site, with δ_{iso} = 58.7 ppm, C_Q = 3.2 MHz and η = 0.2
472 (Kirkpatrick et al., 1985; Phillips et al. 1988; Xiao et al., 1995). The signal at around
473 +63 ppm in Figure 5a is from a Na-feldspar impurity. Similarly, a single Al site is found
474 in the spectrum of low albite with with δ_i = 63.1 ppm, C_Q ~ 3.2 MHz and η = 0.65
475 (Kirkpatrick et al., 1985; Phillips et al. 1988). Note that the same C_Q value is used for

476 the two simulations. However, the high sanidine spectrum is more compatible with the
477 presence of broad distributions of tetrahedral sites for aluminum.
478
479 Figure 6a shows the changes in the C.T. of spectra with Si, Al disorder at 9.4 T
480 along the order-disorder series. The slightly disordered structures of intermediate
481 microcline show the same quadrupolar lineshape structure from the T_1O site as low
482 microcline (specimen *11924* in Fig. 5a and specimen *9544* in Fig. 6a), but it is
483 somewhat blurred (marked with 1, 2 and 3 in specimen *116*). In this case, an additional
484 shoulder at 61 ppm (marked as 4) is also detected. As disorder increases, the signal at
485 61 ppm increases, but the quadrupolar profiles cannot be recorded. In the high sanidine,
486 a broad asymmetric signal is obtained, with a maximum between the signals 1 and 4.
487 Figure 7 displays the variation of the first moment M_1 of the C.T., calculated between
488 35 and 70 ppm, versus the linewidth at the middle height at this low external magnetic
489 field. The M_1 and linewidth values change from 53.3 and 8.1 ppm in low microcline
490 (specimen *11924*) to 57.1 ppm (sample *7294*) and 13.0 (specimen *EU2*) in high
491 sanidine. This observed dispersion of data is due to variable contribution of the two
492 components T_1 and T_2, but also to the influence of Na atoms in the solid solution as well
493 as to Na-feldspar impurities caused by exsolution. However, it clearly shows the
494 existence of two populations of different K-feldspars, one consisting of microcline and
495 orthoclase, and the other, of sanidine and valencianite, which reflect different local
496 structures. The second population shows a higher dispersion of values, but if natural
497 *EU2* and *713r* specimens are ion-exchanged to produce pure K-feldspar as *K-EU2* and
498 *K-713r** synthetic samples, the M_1 value is displaced from 13.0 and 12.7 ppm to 11.7
499 ppm. This value is very similar to that of the synthetic *7294* sample. Such type of
500 displacement is much smaller in ion-exchanged orthoclase (*K-ASGS*).

501

502 At 19.6 T, the C.T. signals from Al atoms are narrower than at 9.4 T (Fig. 6b)
503 displaying again two signals from T_1 and T_2 sites. In specimen *9544*, the quadrupolar
504 broadening at 19.6 T (marked with 1 and 2) is lower but can be simulated with
505 comparable quadrupolar parameters as those used in specimen *11924* at 9.4 T. The
506 increment of local disorder produces the appearance of an additional signal at the left
507 side of the main peak, as at 9.4 T (marked with "4" for specimen *116*). The ^{27}Al spectra
508 at 19.6 T were simulated with a quadrupolar line for the T_1 sites and a Gaussian curve
509 for the T_2 sites, both signals becoming broader with disorder (Table 4). The Al
510 occupancies in these two sites were calculated from their spectral areas as Σt_1 and Σt_2
511 values. In the more disordered samples (natural and ion-exchanged sanidine and
512 valencianite AGM), the best spectral simulations were obtained for $\Sigma t_1 > \Sigma t_2$, with a
513 similar order-disorder parameter as that estimated from the ^{29}Si spectra. The C_Q and η
514 parameter change from circa 3.2 MHz and 0.25 in low microcline to 4.0 MHz and 0.5 in
515 high sanidine, with minor but still detectable changes in the chemical shifts. Note also
516 that disorder was simulated by increasing the linewidths (i.e., the Em parameter) in the
517 ^{27}Al spectra, as it was done also in the simulations of the ^{29}Si spectra.

518

519 The modeling of the quadrupolar parameters for the two sets of T sites is
520 described in Figure 8, for structures close to the ordered and disordered end-members,
521 by means of a "second-order graphic extrapolation" of the chemical shift (similar to the
522 SORGE diagram of Massiot et al. 1995). It shows the external magnetic field
523 dependence of the position of the centers of gravity (cg) for the C.T. from Al atoms in
524 the two sets of T sites. The two T_1 and T_2 sites are represented by two straight lines
525 passing through three points, the δ_{cg} at 9.4 T ($1/\nu_0^2 = 92.02 \times 10^{-4}$ MHz^{-2}), the δ_{cg} at 19.6

526 T ($1/\nu_0^2$ = 21.06 x10^{-4} MHz^{-2}), and the intercept with the vertical axis corresponding to
527 the δ_{iso} corrected from quadrupolar effects. For the T_1O site, the value of δ_{iso} calculated
528 from the spectral simulation and the SORGE diagram are coincident in low microcline.
529 However, the δ_{iso} for the T_2 sites can be inferred only from Figure 8c, as this signal was
530 simulated with Gaussian curves. Thus δ_{iso} (T_2) = 62.1 ppm was estimated for disordered
531 Al atoms (from δ_{cg} = 61.1 ppm at 9.4 T and δ_{cg} = 61.8 ppm at 19.6 T) in intermediate
532 microcline and orthoclase. In addition, the slope of these lines is proportional to ν_Q^2,
533 allowing the calculation of ν_Q for the T_2 sites as ~220 kHz, less than the half of the
534 value at the T_1O site. Similarly, the NMR parameters of the T_2 site in sanidine *EU2*
535 were calculated as δ_{iso} = 62.5 ppm, C_Q = 2.46 MHz ($\nu_Q \approx$ 370 kHz). With these values,
536 we were finally able to simulate the C.T. at both external magnetic fields using two
537 quadrupolar profiles if a η = 0.60 value is used for the T_2 sites (this parameter could not
538 determined from initial simulations using Gaussian profiles).
539
540 **^{39}K MAS NMR spectra**
541 The C.T. of the ^{39}K spectrum of specimen *11924* at 19.6 T (Fig. 9a) shows a
542 single M_1 site for the K atoms, as in the spectrum recorded by Stebbins et al. (2002) for
543 low microcline, with δ_i = 65.2 ppm, C_Q = 1.91 MHz and η = 0.87 (Table 4). The ^{39}K
544 spectrum of specimen 9544 can still be fitted with a single site, but a slightly larger
545 quadrupolar C_Q value is needed to reproduce the profile (Fig. 9a, Table 4). With
546 increasing disorder, this quadrupolar profile becomes blurred, and at least two signals
547 are needed for a simulation of the spectra, corresponding to two sets of
548 spectroscopically distinct M_1 and M_2 sites inside the irregular cavity, instead of a single
549 crystallographic M site as proposed by Taylor's model. Spectra were reproduced with a
550 quadrupolar profile for the M_1 site and a Gaussian curve for the M_2 site, with changes in

551 the line broadening and in asymmetry parameter η from 0.87 in low microcline to
552 values around 0.6 in valencianite and sanidine for the M_1 site. Also, it is necessary to
553 increase the relative intensity of the M_2 signal, without much change in their chemical
554 shift (in comparison with estimated uncertainties). Disorder is also accompanied by an
555 increase in the linewidths (i.e., the *Em* parameter in spectral simulations). The site
556 occupancies of the K atoms in these M_1 and M_2 sites were calculated from their
557 respective areas as Σm_1 and Σm_2 values. Figure 10 is a correlationship between the site
558 occupancies of framework sites by Al atoms and the cavity sites by K atoms, calculated
559 from areas of the experimental spectra at 19.6 T. A linear relationship is clearly
560 obtained along the order-disorder series.
561
562 **^{23}Na MAS NMR spectra**
563 The C.T. of the ^{23}Na spectra of selected specimens at 19.6 T are shown in Figure
564 9b. The NMR parameters of the simulated peak shapes are given in Table 4. The spectra
565 of untwinned and twinned low microcline are similar at 9.4 T, but they are slightly
566 different at 19.6 T. Spectra from specimen *11924* are compatible with a single M_1 site
567 for Na atoms, with well-defined quadrupolar parameters, whereas an additional signal
568 from the M_2 site is detected in specimen *9544*. This signal from the M_2 site does not
569 overlap with a broad signal from the Na atoms of Na-feldspar in exsolution lamellae
570 and impurities (marked with an asterisk in specimen *11924*, Fig. 9). Na-feldspar is
571 absent in sanidine *EU2* and valencianite *AGM* as shown in spectra of Figure 9b. Again,
572 all the spectra were simulated with a quadrupolar profile for the M_1 site and a Gaussian
573 curve for the M_2 site. With disorder in the Si, Al distribution, the relative area of the
574 signal from Na atoms in the M_2 site increases, displaying similar Na occupancies in the
575 two sites in spectra obtained at 9.4 and 19.6 T. In general terms, the simulation of the

576 ^{23}Na spectra is also consistent with that of ^{39}K spectra, giving comparable Σm_1 and Σm_2
577 occupancies. The relationship between the occupancies of framework sites by Al atoms
578 and cavity sites by Na atoms is parallel to that represented in Figure 10. In other words,
579 no clear segregation of alkali atoms in these sites was noted. However, a strong/sharp
580 increase in the C_Q for the M_1 site, a linewidth increase for the M_2 site, and some peak
581 shifts were noted with progressive disorder, effects that were investigated in detail with
582 the help of the SORGE diagram (Fig. 11). The values of the NMR parameters for the
583 M_1 site from this diagram are also well-matched with those quantities estimated from
584 individual simulations. However, for the M_2 site, the C_Q and δ_{iso} parameters can only be
585 estimated from the SORGE diagram, using the δ_{cg} values measured from the Gaussian
586 profiles of the spectral simulations to calculate the ordinate for x = 0 and the line slopes.
587 In this way, δ_{iso} at -20.3 and -18.7 ppm and C_Q of 1.07 and 1.46 MHz were obtained for
588 the M_2 sites in low microcline and high sanidine, respectively. Using these values, the
589 quadrupolar profiles for the M_2 site were reasonably reproduced for $\eta \approx 0.70$ in the
590 original spectra at both external magnetic fields.
591
592 **DISCUSSION**
593 **Local structures in K-feldspar**
594 Structural states in K-feldspar are conventionally defined between two end-
595 members or stable thermodynamic phases: low microcline for the fully ordered end-
596 member and high sanidine for the totally disordered end-member. These states are
597 described with very specific lattice models from reciprocal-space techniques. Orthoclase
598 is generally considered to be an intermediate and metastable state, whereas valencianite
599 is described as an unstable phase (Smith 1974).
600

Figure 12a exhibits the triclinic *C*-1 model of low microcline, in which the four T sites have a fixed Al occupancy defined as $t_1O = 1.0$ and $t_1m = t_2O = t_2m = 0.00$, and a single M site for K atoms. Two structural layers are schematically represented, with four four-membered rings of tetrahedra, labeled 1 to 4, in two complementary orientations (bottom left and right schemes, Fig. 12a). The ring structures have perfect alternation in the number of Al atoms (in red color) per ring, shown as "…-2-0-2-0-…" chains along the b axis (as well as perpendicularly) in the upper layer and "…-0-2-0-2-.." in the lower layer. A coordination of the K atom by seven oxygen atoms emerges for K-O distances less than ~3.0 Å (Downs et al. 1996). Two K-O_{CO} bonds exist here in each four-T ring with two Al atoms (one in dark red related to the K_u atom if this bond points up, the other in light red at the K_d atoms when it points down, O_{CO} atoms in red color). The K-O_{Cm} distances are greater than 3.12 Å (discontinuous lines and oxygen atoms in black color), and thus O_{Cm} atoms are underbonded with K atoms. The NMR data of the untwinned low microcline (specimen *11924* with $t_1O = \Sigma m_1 = 1.0$ and $t_2m \approx t_2o \approx t_1m \approx \Sigma m_2 = 0.00$) are entirely consistent with that model to produce perfect long-range periodicity. The non-equivalent crystallographic sites, defined with invariant atomic coordinates from the average structure after Bragg diffractions, are equivalent to spectroscopically distinct sites in the form of specific local chemical environments with fixed quadrupolar parameters and chemical shifts from NMR spectra.

Figure 12b shows two structural layers of tetrahedra of the monoclinic *C*2/m model of high sanidine ($t_1O = t_1m = t_2O = t_2m = 0.25$), in which the mirror plane "m", twofold "2" axes and inversion centers are schematically represented. The rings do not show the Si and Al occupancies (i.e., the two shown in green) and the cavity atoms rest in a single M site located at the mirror plane, for a random distribution of the framework

626 cations. In other words, the ionicity of the K atoms and the monoclinic symmetry for the
627 topology of tetrahedra were formally linked in Taylor's original model to describe
628 structural disorder. The K-O_C distances are larger than 3.12 Å, and thus, O_C atoms (in
629 black) are underbonded (discontinuous lines) by the K atoms, although a coordination
630 with seven oxygen atoms exists from K-O distances lower than ~3.02 Å (as it was used
631 for microcline in Fig. 12a). Substitutional disorder in the framework could be associated
632 with positional disorder inside the cavity.
633
634 Our data support structural features and constraints not fully recognized in this
635 conventional model for disorder, as follows. Two T sites and a single M site were not
636 detected by NMR experiments. The ^{29}Si spectra at 9.4 T and the ^{27}Al spectra at 19.6 T
637 have shown in all cases $\Sigma t_1 > \Sigma t_2$ if the Al occupancies are inferred from the relative
638 areas of peaks. The chemical shifts of the T_1 and T_2 sites in the ^{29}Si and ^{27}Al spectra are
639 equivalent when the same chemical environment is compared, i.e., $(\delta T_1O + \delta T_1m)/2 <$
640 $(\delta T_2O + \delta T_2m)/2$ for Si atoms, and $\delta_{iso}\, T_1 < \delta_{iso}\, T_2$ for Al atoms. The lower C_Q value
641 for Al atoms in T_2 sites (Fig. 8c) could indicate that this site is locally less distorted than
642 the T_1 site. The η parameter for the T_1 sites decreases slightly from sanidine to
643 microcline, indicating lower distortions in these sites with increasing disorder. Thus the
644 T_1 and T_2 sites are very different from the spectroscopic point of view. All of these data
645 unequivocally indicate that random disorder of the framework cations must be very
646 uncommon or nonexistent. Positional disorder involves slightly variable bond-distances
647 and bond-angles, which cause distributions of isotropic chemical shifts and quadrupolar
648 parameters produced by electric field gradients (EFG), as we also noted in the NMR
649 spectra of the alkali cations.
650

651 The simulations of the ^{29}Si spectra can be used to calculate a mean local
652 obliquity Δ from the chemical shifts of the different sites with the same chemical
653 environment; for instance, for T_x (3Si,1Al) we can define Δ as [(δT_1O - δT_1m) + (δ
654 T_2O - δT_2m)] / 2. We have found that in intermediate microcline close to the low
655 microcline (specimen *176*) Δ is 1.85 ppm; in orthoclase Δ is 1.5 ppm, and in sanidine
656 and valencianite Δ is 1.35 ppm. A Δ value of 0.0 must occur for strictly monoclinic
657 symmetry where $\delta T_1O = \delta T_1m$ and $\delta T_2O = \delta T_2m$ (as in models shown in Figs. 2c and
658 4c), but this was not observed in any of the experimental spectra. This finding implies
659 that analogous triclinic-like distortions exist for all structures along the order-disorder
660 series at room temperature, with four spectroscopically distinct T sites having $t_1O \neq t_1m$,
661 $t_2O \neq t_2m$, instead of two T sites for sanidine and four T sites for microcline.
662
663 The ^{39}K and ^{23}Na spectra demonstrate the existence of a single M site for alkali
664 atoms only in untwinned low microcline close to the stoichiometric $KAlSi_3O_8$
665 composition, which is extremely rare in Nature. Two sets of M site distributions can be
666 resolved if some disorder exists in the framework of tetrahedra. The C_Q parameter for
667 the M_1 site derived from the ^{39}K spectra do not change significantly along the order-
668 disorder series, whereas the same parameter for the T_1 site from the ^{27}Al spectra clearly
669 increases. It could indicate similar local environments for K atoms but growing
670 tetrahedral distortions when disorder increases. Thus, the local geometry of the
671 framework cations seems to be forced to change to accommodate framework disorder,
672 whereas the local geometry in the M_1 site for K atoms is better preserved. The same
673 adaptive behavior to disorder is found for Na atoms as the C_Q values from the ^{23}Na
674 spectra increase progressively from low microcline to high sanidine. In addition, the
675 SORGE diagrams indicate C_Q (T_1) > C_Q (T_2) from ^{27}Al spectra as C_Q (M_1) > C_Q (M_2)

676 from ^{23}Na spectra, with similar η parameter in all cases. Note also that δ_{iso} for Na atoms
677 in M_1 sites is lower than in M_2 sites, as can also be inferred for the K atoms. Hence, the
678 NMR data show a remarkable internal consistency if data from the different nuclides are
679 compared. In addition, no segregation of alkali atoms in the M sites is noted.
680
681 Structural models featuring an alkali site split into two half-occupied or four
682 quarter-occupied sites have been proposed for disordered Na-feldspar (Ribbe et al.
683 1969, Prewitt et al. 1976, Winter et al. 1979), hypersolvus alkali feldspars (Fenn and
684 Brown 1977; Salje 1986), disordered Li-feldspar (Baur et al. 1996), as well as in
685 plagioclase (Fitz Gerald et al. 1986) on the basis of the highly anisotropic shape of the
686 electron-density distribution surrounding alkali atoms in single-crystal XRD
687 refinements. Because of the domain structure in some of these disordered feldspars and
688 the limited resolution of diffractometric techniques, non-equivalent positions for alkali
689 atoms are difficult to distinguish from spatial average effects due to slightly disoriented
690 domains. As a result, it is hard to distinguish site distributions from positional disorder
691 of discrete structural sites with XRD techniques. Because the NMR measurements are
692 not averaged over domains or twin microstructures at the mesoscale, which are totally
693 absent in valencianite and sanidine, we can conclude that split sites for alkali atoms
694 must be considered also in disordered K-feldspars.
695
696 If we correlate the site occupancy of framework and cavity cations on the basis
697 of ^{27}Al, ^{39}K and ^{23}Na spectra at 19.6 T, a linear relationship is outlined along the entire
698 order-disorder series (Fig. 10). In addition, the increase in the C_Q values for Al atoms at
699 the T_1 and T_2 sites with framework disorder is also correlated with the same trend for
700 the Na atoms in the M_1 and M_2 sites, indicating the increment of disorder. The departure

from overall monoclinic symmetry at a local scale thus is connected with multi-site correlations or chemical coupling between Al atoms and alkali atoms to form molecular-like Al(T_2)-O-K(M_2) and Al(T_1)-O-K(M_1) linkages. Hence, "real" M sites with energy minima inside a single type of irregular cavity for the alkali atoms are formed as requirements of the Si, Al distribution, as a consequence of local charge-balancing mechanism at the atomic scale. On this basis, a general model for disordered structures can be proposed with a quasi-triclinic local symmetry (i.e., the two-fold axis, the mirror plane and the inversion centers are absent at the medium-range scale) as in Figure 12c. The Al atoms (in red) are distributed over different four-T rings related to O_{CO} or O_{Cm} oxygen atoms (also in red), which are bonded with K atoms. Where Al atoms are at T_1 sites, K_1-O are formed (red arrows), where Al atoms are at T_2 sites K_2-O bonds exist (blue arrows), with overall maintenance of the seven coordination of K by oxygen atoms.

Medium-range order in disordered K-feldspar

The crystal structures of long-range disordered K-feldspars can be described by the ring structures over medium-range length scale, with structural correlations in the range of 0.5 – 2.0 nm according to the number of Al atoms per each four-T ring, which is closely associated with the disposition of the alkali atoms. The medium-range order (MRO) of K-feldspar explains their diversity in two broad groups, microcline and orthoclase on the one hand, and valencianite and sanidine on the other hand.

Microcline. Some disorder is detected only in the ^{23}Na spectrum in regularly twinned low microcline (specimen *9544*). It may be associated with structural distortion at Na-rich broad twin boundaries (Sánchez-Muñoz et al. 1998, Sánchez-Muñoz et al. 2006b).

Intermediate microcline has a more disordered structure, and the simulations of the ^{29}Si spectra are consistent with $t_1O >> t_2m > t_2O \approx t_1m$ values. Interestingly, a high t_1O value seems to be associated with a very low t_1m value (a characteristic that is developed more clearly in orthoclase), but a structure of "…-2-0-2-0-…" chains with "Al(T_1O)-Si(T_2m)-Al(T_1O)-Si(T_2m)" rings must be a major feature.

This framework arrangement does not follow Dempsey's rule that, based on electrostatic arguments, suggests the number of Al-O-Si-O-Al linkages tend to a minimum (i.e., the Al atoms assume the largest possible separation) for a given Si/Al ratio value (Dempsey et al. 1969). Thus, the microcline structures could be analogous to that of hydrogen faujasite where two Si atoms and two Al atoms also form four-membered rings with Si-O-Al bridges at opposite sides, with local stabilization by bonded protons at the bridging oxygen atoms (Schröder and Sauer 1993).

Orthoclase. The ^{29}Si spectra are consistent with $t_1O > t_2m > t_2O \approx t_1m$ with $t_1O + t_2m \approx 0.9$, i.e., our findings imply that Al atoms are preferentially located at T_1O-T_2m-T_1O-T_2m rings. A relatively high Al content at the T_2m site has not been suggested from XRD methods in orthoclase, as only T_1 and T_2 sites are distinguished in the structural lattice model with monoclinic symmetry. However, mean T_2m-O distances larger than the T_2O-O and T_1m-O distances do exist in high albite (Taylor 1965). It is not possible to discriminate between different Al occupancies of the T sites and intrinsic structural differences in these sites on the basis of X-ray data only (Winter 1979). Because of Loewenstein's rule of Al-O-Al avoidance, Al atoms cannot occupy T_1O and T_1m sites in the same four-T ring, and consequently two types of rings with "…-2-0-2-0-…" arrangements must alternate along the chains of tetrahedra as "Al(T_1O)-Si(T_2m)-

751 Al(T_1O)-Si(T_2m)" (rings 1 to 4 in Fig. 12a) and "Si(T_1O)-Al(T_2m)-Si(T_1O)-Al(T_2m)"
752 (rings 1 to 4 in Fig. 12c).
753
754 The natural abundance and persistence of orthoclase in igneous, metamorphic
755 and hydrothermally affected rocks, have been interpreted as resulting from a small
756 driving force for ordering once structural modulations are formed, involving the
757 formation and coexistence of ordered and anti-ordered domains (Eggleton and Buseck
758 1980) and a domain-texture barrier effect (Brown & Parsons 1989). However, it is
759 difficult to imagine extended ordering processes at the subsolidus stage in K-feldspar of
760 hydrothermal origin, because of the low temperature of crystallization. In this case, the
761 observable state of order must be very close to that originally formed during growth.
762 One can envision that it will be very difficult to reverse configuration of atoms where
763 the Al occupancy forms that type of four-T rings, because the ordering reactions cannot
764 occur by a single atomic jump, as an Al atom at the T_2m site avoids the location of
765 another Al atom at the T_1O site in the same four-T ring. Therefore, this particular
766 medium-range order scheme (orthoclase in Fig. 12c) can explain the metastability,
767 attainability and preservation of orthoclase, in spite of the presence of H_2O in the
768 environment.
769
770 *Valencianite*. The ^{29}Si spectra in this type of K-feldspar are compatible with $t_1O > t_2O >$
771 $t_1m \approx t_2m$ values in the less strongly disordered samples and $t_1O > t_2O \approx t_1m \approx t_2m$
772 values in the more strongly disordered ones. However, the (3Si,1Al) and (2Si,2Al)
773 environments seem to be much more abundant than in a simple model obeying
774 Loewenstein's rule. Therefore, the most characteristic feature of valencianite is the
775 expression of some Si, Al order (involving strong deficiency of Si atoms in Q^4

(4Si,0Al), (1Si,3Al) and (0Si,4Al) environments) not accounted for in a conventional disorder model, which assumes purely random distribution of Si and Al neighbors once Loewenstein's rule is respected. This particular order, in such low-temperature structures, is compatible with a medium-range scale configuration in which mainly only one Al atom occurs per four-T rings to give "…-1-1-1-1-…" chains as in rings 5 to 8 in Figure 12c.

Sanidine. The ^{29}Si spectra of natural specimens and synthetic samples are also compatible with $t_1O \neq t_1m$ and $t_2O \neq t_2m$, with a t_1O value higher than the Al occupancy of the other three sites, involving triclinic-like local distortions as noted from the chemical shifts. Loewenstein's rule of Al-O-Al avoidance seems to be respected, as in other framework aluminosilicates (Klinowski et al. 1982, Phillips and Kirkpatrick 1995). However, the (4Si,0Al) and (0Si,4Al) environments are less developed in experimental than in the simulated spectra, which are closer to experimental ones than in the case of valencianite. Hence, the "…-1-1-1-1-…" chain configuration could be still valid for this high-temperature structure, although the additional effect of dispersion of charges seems to be less well developed than in valencianite. In our interpretation, sanidine forms directly as a quasi-triclinic modification, or it undergoes displacive-like transformations on cooling, or both. Extensive Si, Al ordering on cooling cannot be invoked in unexsolved natural Na-rich specimens and in samples obtained via ion-exchange experiments.

IMPLICATIONS

Two complementary implications are derived from previous experimental data, one at the level of K-feldspar systematics and nomenclature, the other related to the own understanding of the crystalline solid-state.

The IMA only recognizes three terms for K-feldspar mineral species, namely sanidine, orthoclase and microcline (Barth 1934). However, "valencianite" can be described with a crystal structure having not only the distinctive characteristics of triclinicity and disorder, but also a particular MRO atomic scheme, as suggested from the NMR data of this work. Thus, perhaps "valencianite" can be considered also as a mineral species of the K-feldspar group. This K-feldspar must be of high interest in the study of authigenic rocks and mineral deposits from epithermal environment.

Solids are commonly seen from a sharp twofold perspective, either as crystalline or non-crystalline, having (or not) atomic order on a scale that produces an indexable diffraction pattern (IUCr 1992, Nickel 1995). In crystalline solids, short-range order (SRO) arises from atomic forces resulting in the first sphere of coordination, whereas long-range order (LRO) is the consequence of periodicity (Lifshitz 2007). Where crystals have perfect LRO (i.e., the distances of atomic correlations are much longer than the size of coherent diffraction), reciprocal-space techniques are able to resolve structural arrangements at the atomic scale as lattice models in "ideal" crystal structures.

However, the discovery of quasicrystals involves the unequivocal existence of solids with LRO without periodicity, and led to the modern debate of *what is a "crystal"* (Desiraju 2003, Lifshitz 2007). In addition, it is worth considering to what

826 extent the concept of space group needs to be amended in disordered structures
827 (Welberry 2004). Disordered, modulated and incommensurated crystals have strictly
828 non-periodic structures and site distributions, but their "real" structure can in principle
829 be described with a periodic "ideal" average from the analysis of the concentrated
830 intensity at Bragg peaks (i.e., ignoring diffuse scattering).
831
832 Feldspars (the most abundant minerals in the crust of the Earth and Moon) are
833 particularly relevant in this debate because: i) disorder was expressed in terms of a
834 periodic average structure for the first time in sanidine by XRD (Taylor, 1933); ii) the
835 modulated and incommensurated structures of feldspars are currently described using
836 the concept of an average structure (Taylor 1965, Ribbe 1984, Ribbe 1994), and iii)
837 diffuse scattering is ubiquitous (Laves 1950, Gay 1953, Jagodzinski 1984, Pleger 1996).
838 We have shown in the present study that the NMR data cannot be interpreted with
839 available lattice models where long-range disorder exists. *Major* substitutional Si, Al
840 disorder in T sites is not coupled only with *minor* positional disorder for K atoms inside
841 the irregular cavity in a K-feldspar. Non-equivalent atoms and site distributions due to
842 positional disorder are both superposed at the same lattice site in the overlapped image
843 offered by XRD, owing to a lack of intrinsic spatial resolving power. More importantly,
844 the average structure approach in strictly non-periodic disordered crystals fails to
845 recognize essential chemical medium-range order (MRO), i.e., "real" structural features
846 at the local scale can be hidden if "ideal" long-range periodicity is imposed. Obviously,
847 the lattice model is unsuccessful to describe crystallinity based on MRO schemes that
848 do not form extended periodic arrangements.
849
850 **ACKNOWLEDGMENTS**

This work was partially supported by the National High Magnetic Field Laboratory through National Science Foundation Cooperative Agreement (DMR-0084173) and by the State of Florida. LSM thanks projects MAT2010-21088-C03-01 and MAT2010-17753 for additional financial support. We thank Francois Delbove for sample *7294*, Ray Berry for specimen *11924*, and Museo Geo-Minero (IGME) in Madrid, Museo Nacional de Ciencias Naturales (MNCN, CSIC) of Madrid, and Museé d'Histoire Naturelle de Paris, for the K-feldspar specimens used in this work. We also thank to Mr. Olivier Rouer (ISTO, CNRS, France) for the results of the EMPA chemical analyses. In addition, we thank Robert F. Martin and two anonymous reviewers for the suggestions and constructive comments, as well as associate editor Brian Phillips for their help in improving this work.

REFERENCES CITED

Anbalagan, G., Sankari, G., Ponnusamy, S., Thilak Kumar, R., and Gunasekaran, S. (2009) Investigation of silicate mineral sanidine by vibrational and NMR spectroscopic methods. Spectrochimica Acta Part A: Molecular and Biomolecular Spectroscopy, 74, 404-409.

Akizuki, M. and Sunagawa, I. (1978) Study of sector structure in adularia by means of optical microscopy, infra-red absorption, and electron microscopy. Mineralogical Magazine, 42, 453-462.

Bambauer, H.U., Krause, C., and Kroll, H. (1989) TEM investigation of the sanidine/microcline transition across metamorphic zones: the K feldspar varieties. European Journal of Mineralogy, 1, 47-58.

Barth, T.F.W. (1934) Polymorphic phenomena and crystal structure. American Journal of Science, 227, 273-286.

Baur, W.H., Joswig, W., and Müller, G. (1996) Mechanics of the feldspar framework; crystal structure of Li-feldspar. Journal of the Solid State Chemistry, 121, 12-23.

Blasi, A. (1984) The variation of the 2θ angles in powder diffraction patterns of one- and two-step K-rich feldspars. Bulletin de Minéralogie, 107, 437-445.

Blasi, A., Brajkovic, A., De Pol Blasi, C., Foord, E.E., Martin, R.F., and Zanazzi, P.F. (1984a) Structure refinement and genetics aspects of a microcline overgrowth on amazonite from Pikes Peak batholiths, Colorado, U.S.A. Bulletin de Minéralogie, 107, 411-422.

Blasi, A., Brajkovic, A., and De Pol Blasi, C. (1984b) Dry-heating conversion of low microcline to high sanidine via a one-step disordering process. Bulletin de Minéralogie, 107:423-435

Brown, G.E., Hamilton, W.C., Prewitt, C.T. and Sueno, S. (1974) Neutron diffraction study of Al/Si ordering in sanidine: a comparison with X-ray diffraction data. In W S. MacKenzie and J. Zussman Eds, The Feldspars, p. 68-80, Manchester Univ. Press, Manchester.

900 Brown, W.L. and Parsons, I. (1989) Alkali feldspars: ordering rates, phase
901 transformation and behavior diagrams for igneous rocks. Mineralogical Magazine, 53,
902 25-42.
903
904 Chaison, U. (1950) The optics of triclinic adularia. Journal of Geology, 58, 537-547.
905
906 Dempsey, E., Kuhl, G.H. and Olson, D.H. (1969) Variation of the lattice parameter with
907 aluminum content in synthetic sodium faujasites. Evidence for ordering of the
908 framework ions. Journal of Physical Chemistry, 73, 387-390.
909
910 Desiraju, G.R. (2003) In search of clarity. Nature, 423, 485.
911
912 Downs, R.T., Andalman, A., and Hudacsko, M. (1996) The coordination number of Na
913 and K atoms in low albite and microcline as determined from a procrystal electron-
914 density distribution. American Mineralogist, 81, 1344-1349.
915
916 Eggleton, R.A., and Buseck, P.R. (1980) The orthoclase-microcline inversion: a high
917 resolution transmission electron microscope study and strain analysis. Contributions to
918 Mineralogy and Petrology, 74, 123-133.
919
920 Fitz Gerald, J.D., Parise, J.B. and Mackinnon, I.D.R. (1986) Average structure of an
921 An_{48} plagioclase from the Hogarth Ranges. American Mineralogist, 71, 1399-1408.
922
923 Fenn, P.H. and Brown, G.E. (1977) Crystal structure of a synthetic, compositionally
924 intermediate, hypersolvus alkali feldspar: evidence for Na, K site ordering. Zeitschrift
925 für Kristallographie, 145, 124-145.

Gay, P. (1953) The structures of the plagioclase feldspars: III. An X-ray study of anorthites and bytownites. Mineralogical Magazine, 30, 169-177.

IUCr (1992) International Union of Crystallography: Report of the executive committee for 1991. Acta Crystallographica A**,** 48, p.928

Jagodzinski, H. (1984) Determination of modulated structures. Bulletin de Minéralogie, 107, 455-466.

Keefer, K.D. and Brown, G.E. (1978) Crystal structures and composition of sanidine and high albite in cryptoperthitic intergrowth. American Mineralogist, 63, 1264-1273.

Kimata, M., Saito, S., Shimizu, M., Iida, I., and Matsui, T. (1996a) Low-temperature crystal structure of orthoclase and sanidine. Neues Jahrbuch für Mineralogie Abhandlungen, 171, 199-213.

Kimata, M., Shimizu, M. and Saito, S. (1996b) High-temperature crystal structure of sanidine. The crystal structure of sanidine at 935ºC. European Journal of Mineralogy, 8, 15-24.

Kirkpatrick, R.J., Kinsey, R.A., Smith, K.A., Henderson, D.M., and Oldfield, E. (1985) High resolution solid-state sodium-23, aluminum-27, and silicon-29 nuclear magnetic resonance spectroscopic reconnaissance of alkali and plagioclase feldspars. American Mineralogist 70, 106-123.

Klinowski, J., Ramdas, S., Thomas, J.M., Fyfe, C.A. and Hartman, J.S. (1982) A re-examination of Si, Al ordering in zeolites NaX and NaY. Journal of the Chemical Society, Faraday Transactions 2: Molecular and Chemical Physics, 78, 1025-1050.

Kroll, H., Schmiemann, I., and von Cölln, G. (1986) Feldspar solid solutions. American Mineralogist, 71, 1-16.

Kroll, H. and Ribbe, P.H. (1987) Determining (Al,Si) distribution and strain in alkali feldspars using lattice parameters and diffraction peak positions: a review. American Mineralogist, 72, 491-506

Laves, F. (1950) The lattice and twinning of microcline and other potash feldspars. Journal of Geology, 58, 548-571.

Laves, F. and Goldsmith, J.R. (1961) Polymorphism, order, disorder, diffusion and confusion in the feldspars. Cursillos y Conferencias, 8, 71–80.

Laves, F. and Hafner, F. (1962) Infrared absortion effects, nuclear magnatic resonance and structure of feldspars. Norsk Geologisk Tidsskrift, 42, 57-72

LeBail, A., Duroy, H., and Fourquet, J.L. (1988) Ab-initio structure determination of $LiSbWO_6$ by X-ray powder diffraction. Material Research Bulletin, 23, 447-452.

Lifshitz, R. (2007) What is a crystal? Zeitschrift für Kristallographie, 222, 313-317.

Lippmaa, E., Mägi, M., Samoson, A., Engelhardt, G. and Grimmer, A.-R. (1980) Structural studies of silicates by solid-state high-resolution ^{29}Si NMR. Journal of the American Chemical Society, 102, 4889-4893.

Loewenstein, W. (1954) The distribution of aluminum in the tetrahedra of silicates and aluminates. American Mineralogist, 39, 92-96.

Massiot, D., Müller, D., Hübert, T., Schneider, M., Kengens, A.P.M., Coté, B., Coutures, J.P, and Gessner, W. (1995) Double rotation and magic-angle spinning nuclear magnetic resonance study of ^{27}Al: reexamination of the aluminum borate $9Al_2O_3{\cdot}2B_2O_3$. Solid State Nuclear Magnetic Resonance, 5, 175-180.

Massiot, D., Fayon, F., Capron, M., King, I., Le Calvé, S., Alonso, B., Durand, J.O., Bujoli, B., Gan, Z.H. and Hoatson, G. (2002) Modelling one and two-dimensional solid-state NMR spectra. Magnetic Resonance in Chemistry, 40, 70-76.

McConnell, J.D.C. (1965). Electron optical study of effects associated with partial inversion in a silicate phase. Philosophical Magazine, 11, 1289–1301.

McLaren, A.C. and Fitz Gerald, J.D. (1987) CBED and ALCHEMI investigation of local symmetry and Si/Al ordering in K-feldspars. Physics and Chemistry of Minerals, 14, 281-292.

Megaw, H.D. (1956) Notation for feldspar structures. Acta Crystallographica, 9, 56-60.

Megaw, H.D. (1959) Order and disorder in the feldspars, I. Mineralogical Magazine, 32, 226-241.

Nickel, E.H. (1995) The definition of a mineral. The Canadian Mineralogist, 33, 689-690.

O'Brient, J.D. (1986) Preservation of primary magmatic features in subvolcanic pegmatites, aplites and granite from Rabb Park, New Mexico. American Mineralogist. 71, 608-624

Phillips B.L., Kirkpatrick, J., and Hovis, G.L. (1988) ^{27}Al, ^{29}Si and ^{23}Na MAS NMR study of an Al, Si ordered alkali feldspar solid solution series. Physics and Chemistry of Minerals, 16, 262-275.

Phillips, B.L. and Kirkpatrick, R.J. (1995) High-temperature ^{29}Si MAS NMR spectroscopy of anorthite ($CaAl_2Si_2O_8$) and its P-1 – I-1 structural phase transition. Physics and Chemistry of Minerals, 22, 268-276.

Pleger, S. (1996) Diffuse X-ray scattering of homogeneous potassium-rich low- and high-temperature sanidines. Zeitschrift für Kristallographie, 211, 293-298.

Prewitt, C.T., Sueno, S. and Papike, J.J. (1976) The crystal structures of high albite and monalbite at high temperatures. American Mineralogist, 61, 1213-1225.

Ribbe, P.H., Megaw, H.D., Taylor, W.H., Ferguson, R.B. and Traill, R.J. (1969) The albite structures. Acta Crystallographica, B25, 1503-1518.

Ribbe, P.H. (1983) Chemistry, structure and nomenclature of feldspars. *Rev. Mineral*. 2, 1-19.

Ribbe, P.H. (1984) Average structures of alkali and plagioclase feldspars: systematic and applications. In: Brown, W.L. (ed) Feldspars and Feldspathoids. NATO Adv Stud Inst C137, D. Reidel Publishing Company, pp.1-54,

Ribbe, P.H. (1994) The crystal structures of the aluminium-silicate feldspars. In: Parsons, I. (ed) Feldspars and their reactions. NATO Adv Stud Inst C421 Dordrecht, Boston, London, pp 1-49.

Rodriguez-Carvajal, J. (1993) Recent advances in magnetic-structure determination by neutron powder diffraction. Physica B, 192, 55-69

Rodriguez-Carvajal, J. (2001) Reference Guide, V. 1.9c, Laboratoire Léon-Brillouin (CEA-CNRS), France (2001).

Roisnel, T., and Rodriguez-Carvajal, J. (2001) WinPLOTR: A Windows tool for powder diffraction pattern analysis. In: Delhez, R. and Mittemeijer, E.J. (eds), Materials Science Forum, 378-3, 118-123.

1050 Salje, E. (1986) Raman spectroscopic investigation of the order parameter behavior in
1051 hypersolvus alkali feldspars: displacive phase transitions and evidence for Na-K site
1052 ordering. Physics and Chemistry of Minerals, 13, 340-346.
1053
1054 Sánchez-Muñoz, L., Nistor, L., Van Tendeloo, G., and Sanz, J. (1998) Modulated
1055 structures in $KAlSi_3O_8$: a study by high resolution electron microscopy and ^{29}Si MAS-
1056 NMR spectroscopy. Journal of Electron Microscopy, 47, 17-28.
1057
1058 Sánchez-Muñoz, L., García-Guinea, J., Sanz, J., Correcher, V., and Delgado, A. (2006a)
1059 Ultraviolet luminescence from defects complexes in the twin boundaries of K-feldspar.
1060 Chemistry of Materials, 18, 3336-3342.
1061
1062 Sánchez-Muñoz, L., Correcher, V., Turrero, M.J., Cremades, A., and García-Guinea, J.
1063 (2006b) Visualization of elastic strain fields by the spatial distribution of the blue
1064 luminescence in a twinned microcline crystal. Physics and Chemistry of Minerals, 33,
1065 639-650.
1066
1067 Sánchez-Muñoz, L., Correcher, V., García-Guinea, J., and Delgado, A. (2007)
1068 Luminescence at 400 and 440 nm in sanidine feldspar from original and X-ray-induced
1069 defects. Nuclear Instruments and Methods in Physic Research A 580, 679-682.
1070
1071 Sánchez-Muñoz, L., García-Guinea, J., Zagorsky, V.Ye., Juwono, T., Modreski, P.J.,
1072 Cremades, A., Van Tendeloo, G., De Moura, O.J.M. (2012) The evolution of twin
1073 patterns in perthitic K-feldspar from granitic pegmatites. The Canadian Mineralogist,
1074 50, 989-1024.

Scambos, T.A.; Smyth, R.J.; and McCormick, T.C. (1987) Crystal-structure refinement of high sanidine from the upper mantle. American Mineralogist, 72, 973-978.

Schröder, K.P. and Sauer, J. (1993) Preferred stability of the Al-O-Si-O-Al linkages in high-silica zeolite catalysts. Theoretical predictions contrary to Dempsey's rule. The Journal of Physical Chemistry, 97, 6579-6581.

Sherriff, B.L. and Hartman, J.S. (1985) Solid-state high-resolution ^{29}Si NMR of feldspars: Al-Si disorder and the effect of paramagnetic centres. The Canadian Mineralogist, 23, 205-212.

Smith, J.V. (1954) A review of the Al-O and Si-O distances. Acta Crystallographica, 7, 479-483.

Smith, J.V. (1974) Feldspar minerals, Volume 1, p. 423-436. Springer Verlag, New York.

Smith, J.V., Blackwell, C.S., and Hovis, G.L. (1984) NMR of albite microcline series. Nature, 309, 140-142.

Stebbins, J.F., Du, L.S., Kroeker S., Neuhoff, P., Rice, D., Frye, J., and Jakobsen, H.J. (2002) New opportunities for high-resolution solid-state NMR spectroscopy of oxide materials at 21.1- and 18.8-T fields. Solid State Nuclear Magnetic Resonance, 21, 105-115.

Taylor, W.H. (1933) The structure of sanidine and other feldspars. Zeitschrift für Kristallographie, 85, 425-442.

Taylor, W.H., Darbyshire, J.A., and Strunz, H. (1934) An X-ray investigation of the feldspars. Zeitschrift für Kristallographie, 87, 464-498.

Taylor, W.H. (1965) The Feldspars, in: Crystal Structure of Minerals (W.L. Bragg and G.F. Claringbull, eds.); Bell and Sons, London, UK.

Welberry, T.R. (2004) Diffuse X-ray scattering and models of disorder (IUCr Monographs on Crystallography 16, Oxford Univ. Press, Oxford.

Winter, J.K.; Okamura, F.P. and Ghose, S. (1979) A high-temperature structural study of high albite, monalbite, and the analbite→monalbite phase transition. American Mineralogist, 64, 409-423

Xiao, Y., Kirkpatrick, R.J., Hay, R.L., Kim, Y.J. and Phillips, B.L. (1995) Investigation of Al, Si order in K-feldspars using ^{27}Al and ^{29}Si MAS NMR. Mineralogical Magazine, 59, 47-61.

Zhou, L., Guo, J., Yuan, H., and Li, L. (1994) Solid state nuclear magnetic resonance and infrared spectroscopy of alkali feldspars. Science in China (Series D), 40, 2, 159-165.

Zhou, L. Guo, J, Liu, B, and Li, L. (2001) Structural state of adularia from Hishikari, Japan. Chinese Science Bulletin, 46, 950-953.

FIGURE CAPTIONS

Figure 1. The ^{29}Si MAS NMR spectra of microcline at 9.4 T, with spectral simulations (sim) resulting from the additions of four components (T_1O, T_1m, T_2O, T_2m), with five chemical environments as Si Q^4(nAl) for n = 0, 1, 2, 3, 4. a) Specimen *9544*, b) Specimen *176*, c) Specimen *116*, and d) Specimen *FB4* (see Table 5 in supporting information online for relative intensities). Symbol "+" for the signal from quartz.

Figure 2. The ^{29}Si MAS NMR spectra of orthoclase at 9.4 T with spectral simulations as in Figure 1. a) Spectrum in natural orthoclase (specimen *ASGS*) and its ion-exchanged product (sample *K-ASGS*). b) Calculated spectrum for $t_1O = 0.7$, $t_1m = t_2O = 0.05$, $t_2m = 0.2$ (see Table 5 in supporting information online for relative intensities). c) Calculated spectra for two-step orthoclase with monoclinic symmetry for $t_1O = t_1m = 0.4$ and $t_2O = t_2m = 0.1$ d) Calculated spectra for one-step orthoclase with triclinic symmetry $t_1O = 0.7$ and $t_1m = t_2O = t_2m = 0.1$ and reduced local obliquity. Table 6 (supporting information online) has the relative peak intensities for each model. Symbol "*" see text for explanation.

Figure 3. The ^{29}Si MAS NMR spectra of valencianite at 9.4 T with spectral simulations as in Figure 1. a) Spectra from specimen *1109* and specimen *1406* in comparison with a calculated spectrum for a triclinic structure with $t_1O = 0.60$, $t_1m = 0.10$, $t_2O = 0.20$ and $t_2m = 0.10$. b) Spectra from specimens 1407 and *AGM* in comparison with a calculated

spectrum for a triclinic structure with $t_1O = 0.40$, $t_1m = t_2O = t_2m = 0.20$. Sim1 and sim2 are built up using different intensities in Table 5 (supporting information online). Symbol "+" for the signal from quartz, and symbol "*" see text for explanation.

Figure 4. The ^{29}Si MAS NMR spectra of sanidine at 9.4 T with spectral simulations as in Figure 1. a) Specimens *EU2*, *SVNI-2, RABB* and *SBKS*, and samples *7294*, *K-713r** and *K-EU2*. b) Calculated spectrum for a sanidine ($t_1O = 0.40$, $t_1m = 0.15$, $t_2O = 0.25$ and $t_2m = 0.20$) with a triclinic structure but reduced local obliquity. c) Calculated spectrum for strict monoclinic symmetry $t_1O = t_1m = t_2O = t_2m = 0.25$. d) Calculated spectrum for triclinic symmetry with reduced obliquity and the same occupancies of c). Symbol "*" see text for explanation.

Figure 5. The ^{27}Al MAS NMR spectra of alkali feldspars at 9.4 T. a) Specimen *11924* or untwinned K-feldspar ordered end-member (low microcline), marked with 1, 2 and 3 for the features of the quadrupolar profile of the T_1O site, simulated with δ_{iso} = 58.7 ppm, C_Q = 3.2 MHz and η = 0.2. b) Specimen *CLBR* with fully ordered low albite, simulated with δ_{iso} = 62.9 ppm, C_Q = 3.17 MHz, and η = 0.65. c) Sample *7294* as the disordered end-member (high sanidine) with $KAlSi_3O_8$ composition.

Figure 6. The ^{27}Al MAS NMR spectra from selected specimens and samples of K-feldspar at 9.4 T in a) and 19.6 T in b). Signals 1, 2 and 3 can be explained as in Figure 5 from T_1 sites, and signal 4 corresponds to Al atoms in T_2 sites. Spectral simulations in b) are performed with NMR parameters of Table 4. Dotted lines for T_1 sites and dashed lines for T_2 sites, simulated spectra as fine continuous lines, experimental spectra as thick continuous lines.

1175

1176 **Figure 7.** Variation of the first moment M_1 with linewidth in ppm from the C.T. in the
1177 ^{27}Al spectra at 9.4 T. The relationships between some natural specimens and their ion-
1178 exchanged counterpart are marked with arrows. Ordered and disordered end-members
1179 (specimen *11924* and sample *7294*) and valencianite *AGM* are also labeled.

1180

1181 **Figure 8**. SORGE diagram for the two spectroscopically distinct sets of T sites for Al
1182 atoms for microcline and sanidine. The δ_{cg} values for the central transition are plotted
1183 with the intensity of the external magnetic field as $1/\nu_0^2$. The T_1 site in microcline from
1184 specimen *9544*, the T_2 site for intermediate microcline from specimen *116*, T_1 and T_2
1185 sites in sanidine from specimen *EU2*, (see explanations in the text) are here analyzed.
1186 The chemical shift values from the simulated spectra are denoted by white symbols,
1187 whereas calculated chemical shift values from this diagram are in grey.

1188

1189 **Figure 9**. The ^{39}K MAS NMR spectra in a) and ^{23}Na MAS NMR spectra in b) of
1190 selected K-feldspars at 19.6 T. Dotted lines for M_1 sites and dashed lines for M_2 sites,
1191 simulated spectra as fine continuous lines (Table 4), experimental spectra as thick
1192 continuous lines. The asterisk "*" denotes signal from exsolved Na-rich feldspar.

1193

1194 **Figure. 10**. Correlationship between Σt_1 from Al atoms in T_1 sites and Σm_1 from K
1195 atoms in M_1 sites from spectral simulations (Table 4) of experimental spectra at 19.6 T.

1196

1197 **Figure 11**. SORGE diagram for the two spectroscopically distinct sets of M sites for Na
1198 atoms, where the δ_{cg} values for the C.T. are plotted with the external magnetic field as

1199 $1/v_0^2$. M_1 and M_2 sites from twinned low microcline (specimen *9544*) and high sanidine
1200 (specimen *EU2*) with symbols as in Fig. 8 (see explanations in the text).
1201
1202 **Figure 12.** Lattice models of low microcline (a) and high sanidine (b) from XRD; "m"
1203 mirror plane, "2" two-fold binary axis, and "*" inversion centers. c) Quasi-triclinic
1204 model with MRO from NMR for orthoclase, valencianite and sanidine. The projection
1205 normal to the *a* axis show two sheets of T sites with the interlayer M sites, and onto the
1206 (001) plane display a chain of T atoms along the *b* axis and related K atoms at different
1207 height. The K-O_{CO} bonds (absent in the monoclinic model) are in red for K_u (up) and
1208 light red for K_d (down). Four 4-membered rings of T sites are marked with numbers in
1209 the two projections. The T_1 sites are in light red and T_2 sites in blue for the *C*2/m model
1210 in b), whereas T_1O sites in red, T_1m sites in pink, T_2O sites in blue and T_2m sites in
1211 green for the *C*-1 model in a); green color for both Si and Al atoms in b), and blue for Si
1212 atoms and red for Al atoms in a); the O_{A1} oxygen atoms are in orange, the other oxygen
1213 atoms are in yellow; oxygen atoms not bonded to K (at larger distances than 3.12 Å) are
1214 in black and with discontinuous lines. In c), the rings 1 to 4 correspond with orthoclase,
1215 and rings 5 to 8 with the valencianite and sanidine, M_1 sites with red arrows, M_2 with
1216 blue arrows. Structural data: Blasi et al. (1984a) for microcline; Kimata et al (1996a) for
1217 sanidine (see text for details).
1218
1219
1220
1221
1222
1223

Table 1. The thirty-three specimens and samples of K-rich feldspar analyzed.

K-feldspars	Chem. Comp.	Locality	*Origin*	*Source*	K-feldspars
11924	$Or_{96.4}Ab_{3.6}$	Pikes Peak, Colorado USA	1	1	MI
9544	$Or_{94.8}Ab_{5.2}$	Pikes Peak, Colorado USA	2	2	MI
176	$Or_{98.0}Ab_{2.0}$	Colmenar Viejo, Madrid, Spain	3	3	MI
116	$Or_{92.9}Ab_{7.1}$	Colmenar Viejo, Madrid, Spain	3	3	MI
FB4	$Or_{91.1Ab8.9}$	Belvis de Monroy, Cáceres, Spain	3	3	MI
5963	$Or_{93.5}Ab_{6.5}$	Valais, Switzerland	4	2	OR
1123	$Or_{92.8}Ab_{7.2}$	Valais, Switzerland	4	2	OR
ASGS	$Or_{90.6}Ab_{9.4}$	St. Gotthard, Switzerland	4	4	OR
K-ASGS	$Or_{100}Ab_{0}$	-	5	4	OR
AFTS	$Or_{90.3}Ab_{9.7}$	Tavebih, Sweden	4	4	OR
172-34	$Or_{87.0}Ab_{13.0}$	Rondadura, Switzerland	4	5	OR
OrtA2b	-	Salzburgo, Austria	4	4	OR
5368	-	Brinstentor, Switzerland	4	2	VA
1406	-	Guttanen, Switzerland	4	2	VA
382	$Or_{98.7}Ab_{1.3}$	Zillerthal, Tyrol, Austria	4	2	VA
1109	$Or_{97.6}Ab_{2.4}$	Zillerthal,Tyrol, Austria	4	2	VA
115-371	$Or_{96.6}Ab_{3.4}$	Marienberg, Germany	4	5	VA
5426	$Or_{97.5}Ab_{2.5}$	Pfunderthal, Tyrol, Austria	4	2	VA
AGM	$Or_{97.5}Ab_{2.5}$	Guanajuato, Mexico	4	4	VA
1407	$Or_{98.0}Ab_{2.0}$	Uri, Switzerland	4	2	VA?
RABB	-	Rabb Park, New Mexico, USA	6	3	SA
SBKS	$Or_{65.5}Ab_{30.2}An_{4.3}$	Baden, Kaisertuhl, Switzerland	7	4	SA
EU2	$Or_{62.3}Ab_{37.5}An_{1.5}$	Idaho, USA	7	3	SA
K-EU2	$Or_{100}Ab_{0.0}An_{0.0}$	-	5	3	SA
SSNI	-	Mt. Somma, Napoles, Italy	7	4	SA
SANCS1	-	Konstenblutten, Czech Republic	7	4	SA
SEE	$Or_{79.9}Ab_{16.2}An_{4.1}$	Los Lobos, Almería, Spain	7	4	SA
SVNI-1	$Or_{69.4}Ab_{28.8}An_{1.8}$	Mt. Vesuvius, Italy	7	4	SA
SVNI-2	$Or_{72.3}Ab_{25.9}An_{1.7}$	Mt. Vesuvius, Italy	7	4	SA
713r	$Or_{78.7}Ab_{21.3}$	Eifel, Germany	7	5	SA
*K-713r**	$Or_{100}Ab_{0.0}$	-	5,8	5	SA
7294	$Or_{100}Ab_{0.0}$	-	9	-	SA
CLBR	$Or_{2.9}Ab_{97}$	Golconda III, MG, Brazil	10	3	AB

Origin: (1) "White cap" or un-twinned single-crystal microcline overgrowth on amazonite in a miarolitic pegmatite, Pikes Peak batholith (CO, USA). (2) Amazonite from a miarolitic pegmatite, also from Pikes Peak batholith. (3) Sample formed from fluids that fill the fractures and pockets in granitic pegmatites. (4) Transparent homogeneous morphological units of adularia habit from hydrothermal veins. (5) Synthetic product by ion-exchange experiments of specimens with KBr. (6) Subvolcanic pegmatites. (7) Single-crystals separated from volcanic rocks. (8) Sample artificially disordered by thermal annealing at 1050 ºC for 7 days. (9) Specimen synthesized at ISTO from a gel with pure $KAlSi_3O_8$ composition that was crystallized at 725 ºC and 3 kbars for 168 hours in hydrothermal conditions. (10) Albite with the cleavelandite habit from a pocket in a granitic pegmatite in Governador Valadares (MG, Brazil). *Sources*: (1) Ray Berry's collection; (2) Collected from Museo Geo-Minero, IGME, Madrid, Spain; (3) Collected by us at their original locality; (4) Collected from Museo Nacional de Ciencias Naturales de Madrid, CSIC, Spain. (5) Collected from Museé d'Histoire Naturelle de Paris (France). MI microcline, OR orthoclase, VA valencianite, SA sanidine and AB albite. Chemical compositions were obtained by EMPA.

Table 2. Lattice cell parameters, Si/Al order parameters, and K-feldspar varieties from XRD patterns

Materials	*a*	*b*	*c*	α	β	γ	V	Σt_1	Δt_1	XRD Varieties
11924	8.582(1)	12.964(1)	7.225(1)	90.65(1)	115.93(1)	87,67(1)	722.3(1)	0.99(1)	1.00(1)	LM
9544	8.581(1)	12.965(1)	7.222(1)	90.64(1)	115.94(1)	87.68(1)	721.9(1)	0.97(1)	0.99(1)	LM
176	8.587(1)	12.966(1)	7.218(1)	90.50(1)	116.00(1)	88.09(1)	721.9(1)	0.93(1)	0.82(1)	IM
1123	8.560(1)	12.972(1)	7.210(1)	90.00	116.02(1)	90.00	719.4(1)	0.89(1)	0.00	OR
AFTS	8.564(1)	12.990(1)	7.204(1)	90.00	115.99(1)	90.00	720.4(1)	0.80(1)	0.00	OR
5368	8.581(1)	13.006(1)	7.199(1)	90.03(1)	116.03(1)	89.86(1)	721.9(1)	0.71(1)	0.06(1)	nc
1406	8.576(1)	13.004(1)	7.190(1)	90.03(1)	116.02(1)	89.85(1)	720.6(1)	0.68(1)	0.06(1)	nc
AGM	8.594(1)	13.024(1)	7.177(1)	90.06(1)	116.07(1)	89.74(1)	721.6(1)	0.54(1)	0.11(1)	nc
1407	8.593(1)	13.000(1)	7.192(1)	90.00	116.02(1)	90.00	722.0(1)	0.71(1)	0.00	LS
*K-713r**	8.605(1)	13.041(1)	7.184(1)	90.00	115.99(1)	90.00	724.6(1)	0.55(1)	0.00	HS
EU2	8.433(1)	13.006(1)	7.170(1)	90.00	116.05(1)	90.00	706.5(1)	0.59(1)	0.00	HS

Σt_1 and Δt_1 values were calculated using the methods of Kroll and Ribbe (1987) from the cell parameters. XRD varieties are HS high sanidine, LS low sanidine, OR orthoclase, IM intermediate microcline, LM low microcline, from Ribbe (1983). Valencianite specimens with an X-ray pattern consistent with triclinic symmetry cannot be classified by using these terms (nc). Values in parentheses are estimated standard deviations in the last decimal place.

Table 3. NMR parameters from simulation of the ^{29}Si spectra

Specimens	*9544*	*176*	*116*	*FB4*	*K-ASGS*	*1406*	*AGM*		*K-EU2*
Linewidth	0.65	0.80	0.90	1.00	1.10	1.00	sim1 1.10	sim2 1.50	1.35
t_1O	1.00	0.89	0.78	0.74	0.70	0.60	0.40	0.40	0.40
t_1m	0.00	0.03	0.05	0.06	0.05	0.10	0.20	0.20	0.15
t_2O	0.00	0.03	0.06	0.09	0.05	0.20	0.20	0.20	0.25
t_2m	0.00	0.05	0.11	0.11	0.20	0.10	0.20	0.20	0.20
δT_1O (ppm)	-	-102.2	-102.2	-102.1	-101.8	-101.7	-101.7	-101.5	-101.7
δT_1m (ppm)	-100.9	-100.8	-100.8	-100.9	-100.7	-100.7	-100.6	-100.2	-100.6
δT_2O (ppm)	-97.8	-97.7	-97.7	-97.9	-97.8	-97.8	-97.8	-97.4	-97.8
δT_2m (ppm)	-95.2	-95.2	-95.2	-95.0	-94.9	-94.9	-94.7	-95.0	-94.7

The letter "t" lowercase is used for the Al content in the T sites, which are named with "T" uppercase. Specimen *AGM* has two spectral simulations: sim1 and sim2 (Fig. 3). δT_x values are given for the T_1O (3Si,1Al), T_1m (3Si,1Al), T_2O (3Si,1Al) and T_2m (2Al,2Si) sites.

Table 4: NMR parameters from simulation of the ^{27}Al, ^{39}K and ^{23}Na spectra at 19.6 T

K-feldspar types		**Microcline**			**Orthoclase**	**Valencianite**		**Sanidine**	
Specimens		*11924*	*9544*	*116*	*1123*	*1406*	*AGM*	*K713r**	*EU2*
Framework cations in tetrahedral T sites									
^{27}Al at 19.6 T									
T_1	δ_{iso} (ppm)	-	59.2	59.8	60.3	60.6	60.7	60.8	61.0
	Em	-	50	65	80	85	85	80	95
	C_Q (kHz)	-	3150	3641	3650	3716	3664	4006	3932
	η	-	0.25	0.35	0.38	0.42	0.52	0.50	0.50
	Σt_1	-	~ 1.00	0.895	0.805	0.689	0.555	0.542	0.558
T_2	Position (ppm)	-	~ 61.1	61.1	61.0	61.4	61.8	61.6	61.7
	Width (ppm)	-	-	3.3	3.5	3.5	3.6	3.6	3.9
	Σt_2	-	~ 0.0	0.105	0.195	0.311	0.445	0.458	0.442
Alkali cations in M sites at irregular cavities									
^{39}K at 19.6 T									
M_1	δ_{iso} (ppm)	-65.2	-55.7	-60.5	-49.8	-62.5	-65.2	-73.2	-80.3
	Em	14	17	25	40	45	50	50	70
	C_Q (kHz)	1911	2032	1953	2101	2048	2151	1830	2037
	η	0.87	0.87	0.85	0.65	0.65	0.65	0.65	0.65
	Σm_1	1.00	~ 1.00	0.852	0.765	0.674	0.566	0.587	0.537
M_2	Position (ppm)	-	-	-90.0	-86.3	-90.2	-98.6	-95.2	-85.56
	Width (ppm)	-	-	62	63.7	62	72	57.2	74.8
	Σm_2	-	-	0.146	0.235	0.326	0.434	0.412	0.463
^{23}Na at 19.6 T									
M_1	δ_{iso} (ppm)	-24.7	-24.9	-23.5	-22.6	-22.4	-21.9	-	-20.1
	Em	80	80	80	80	80	80	-	80
	C_Q (kHz)	1160	1146	1685	1993	2010	2051	-	2136
	η	0.70	0.70	0.60	0.60	0.60	0.65	-	0.60
	Σm_1 (%)	1.00	0.904	0.792	0.787	0.675	0.530	-	0.555
M_2	Position (ppm)	-	-24.7	-22.7	-22.0	-21.9	-21.0	-	-19.9
	Width (ppm)	-	1.5	2.5	3.4	5.4	6.8	-	5.4
	Σm_2	-	0.096	0.208	0.212	0.325	0.470	-	0.445

Estimated uncertainties in the chemical shifts are ±1 ppm for the ^{27}Al and ^{23}Na spectra, and 10 ppm for ^{39}K spectra. Uncertainties are 100 kHz in C_Q, and 0.2 in η parameter of ordered samples. Estimated uncertainties in cation occupancies are ±10 %.

Figure 1

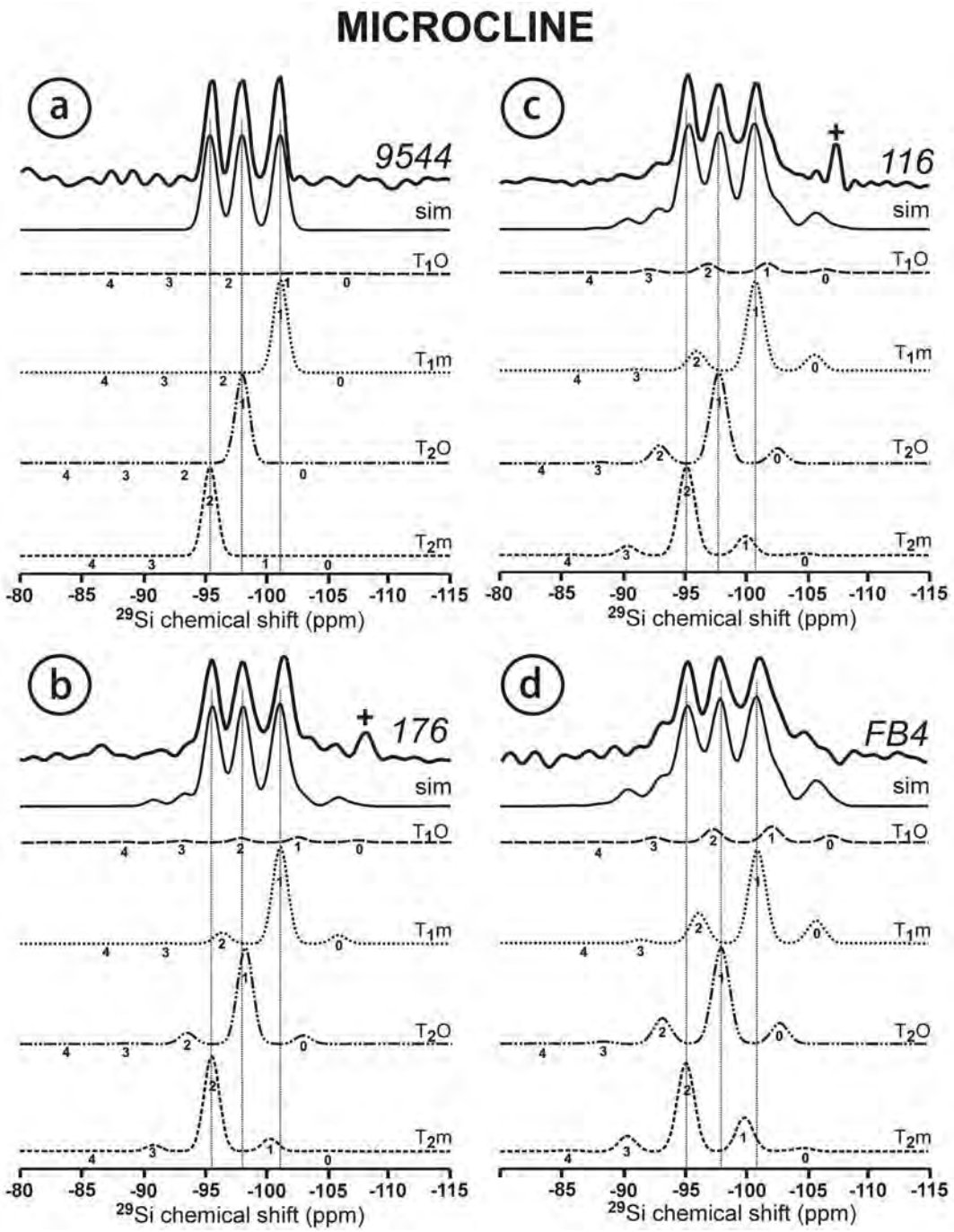
MICROCLINE
a
9544
sim
T1O
T1m
T2O
T2m
-80 -85 -90 -95 -100 -105 -110 -115
29Si chemical shift (ppm)
c
116
b
176
d
FB4

Figure 2

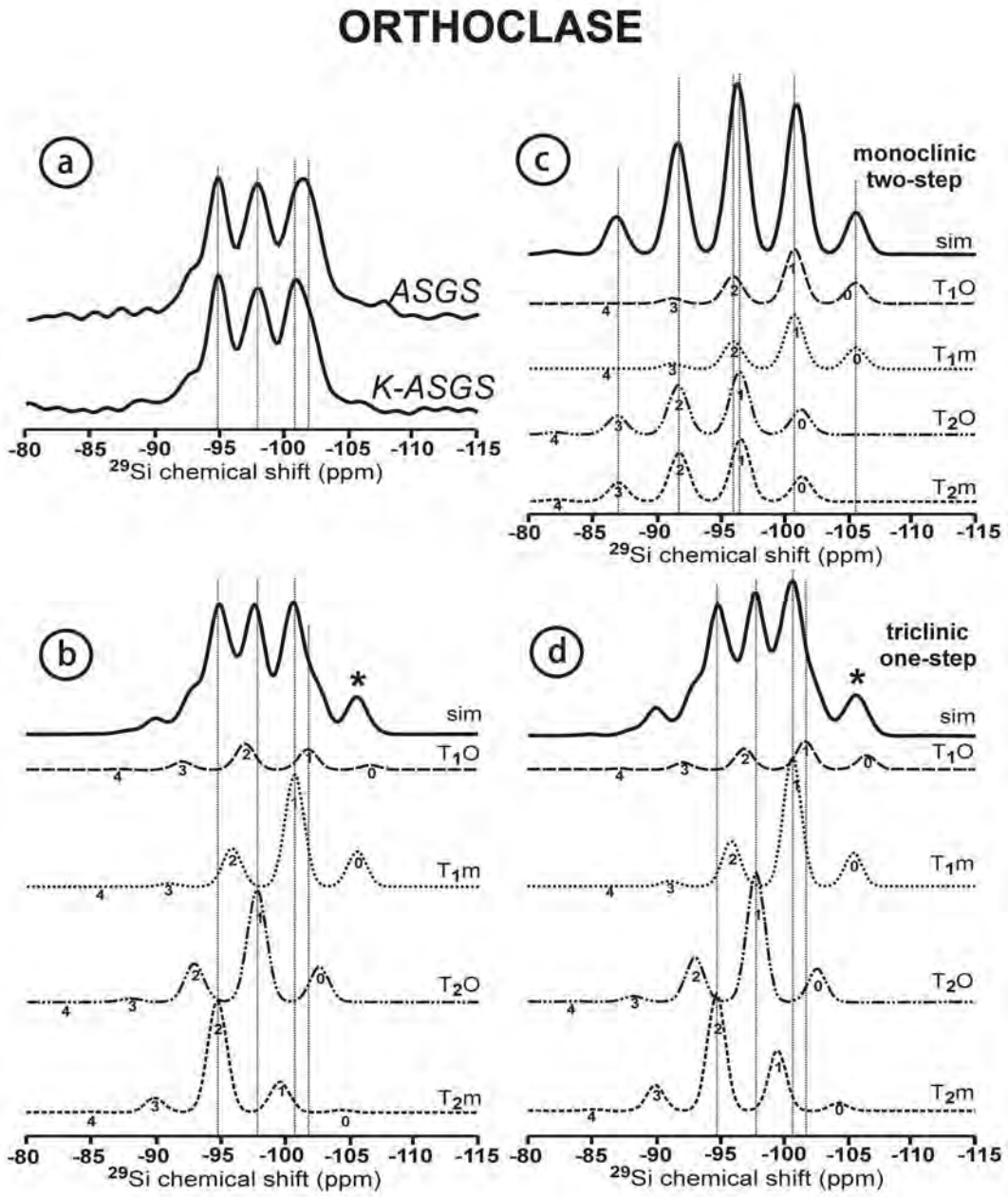
ORTHOCLASE
a
ASGS
K-ASGS
-80 -85 -90 -95 -100 -105 -110 -115
29Si chemical shift (ppm)
c
monoclinic
two-step
sim
T1O
T1m
T2O
T2m
-80 -85 -90 -95 -100 -105 -110 -115
29Si chemical shift (ppm)
b
*
sim
T1O
T1m
T2O
T2m
-80 -85 -90 -95 -100 -105 -110 -115
29Si chemical shift (ppm)
d
triclinic
one-step
*
sim
T1O
T1m
T2O
T2m
-80 -85 -90 -95 -100 -105 -110 -115
29Si chemical shift (ppm)

Figure 3

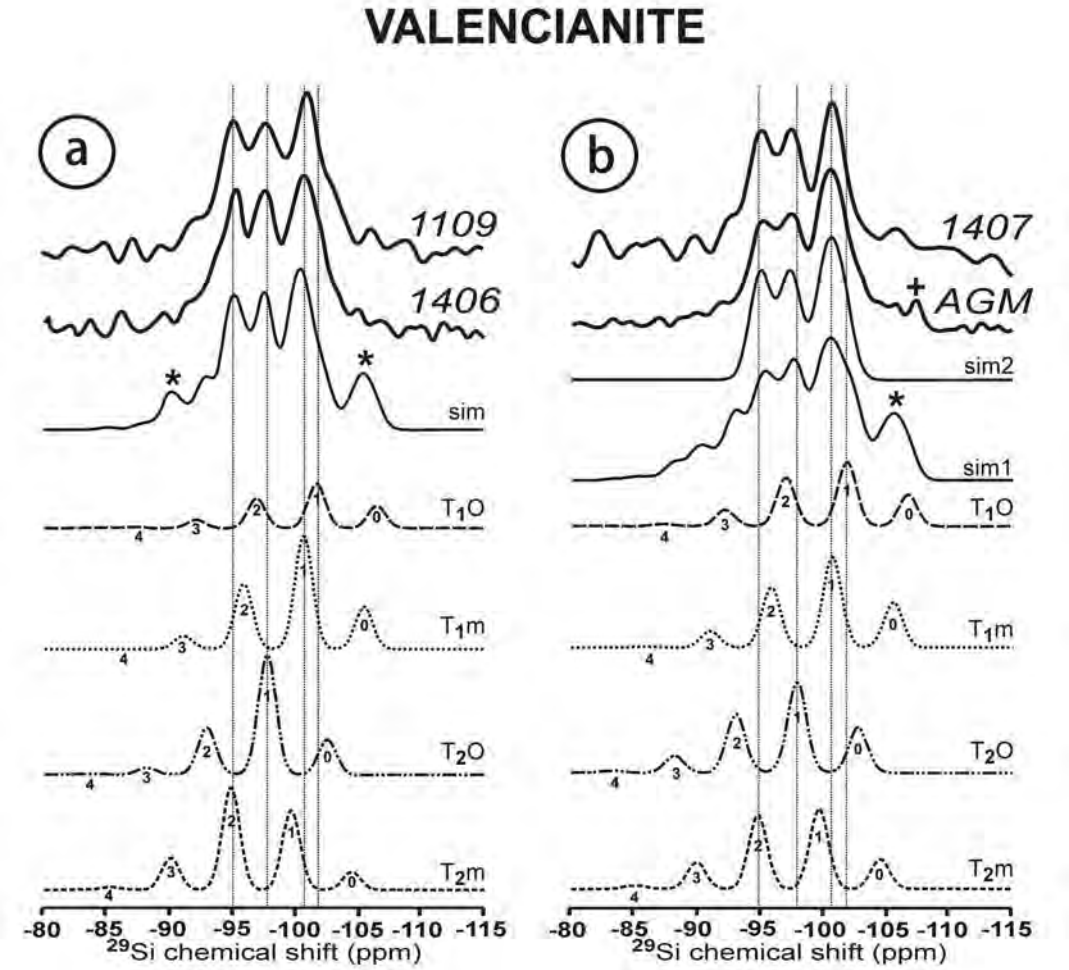
VALENCIANITE
a
1109
1406
sim
T1O
T1m
T2O
T2m
-80 -85 -90 -95 -100 -105 -110 -115
29Si chemical shift (ppm)
b
1407
AGM
sim2
sim1
T1O
T1m
T2O
T2m
-80 -85 -90 -95 -100 -105 -110 -115
29Si chemical shift (ppm)

Figure 4

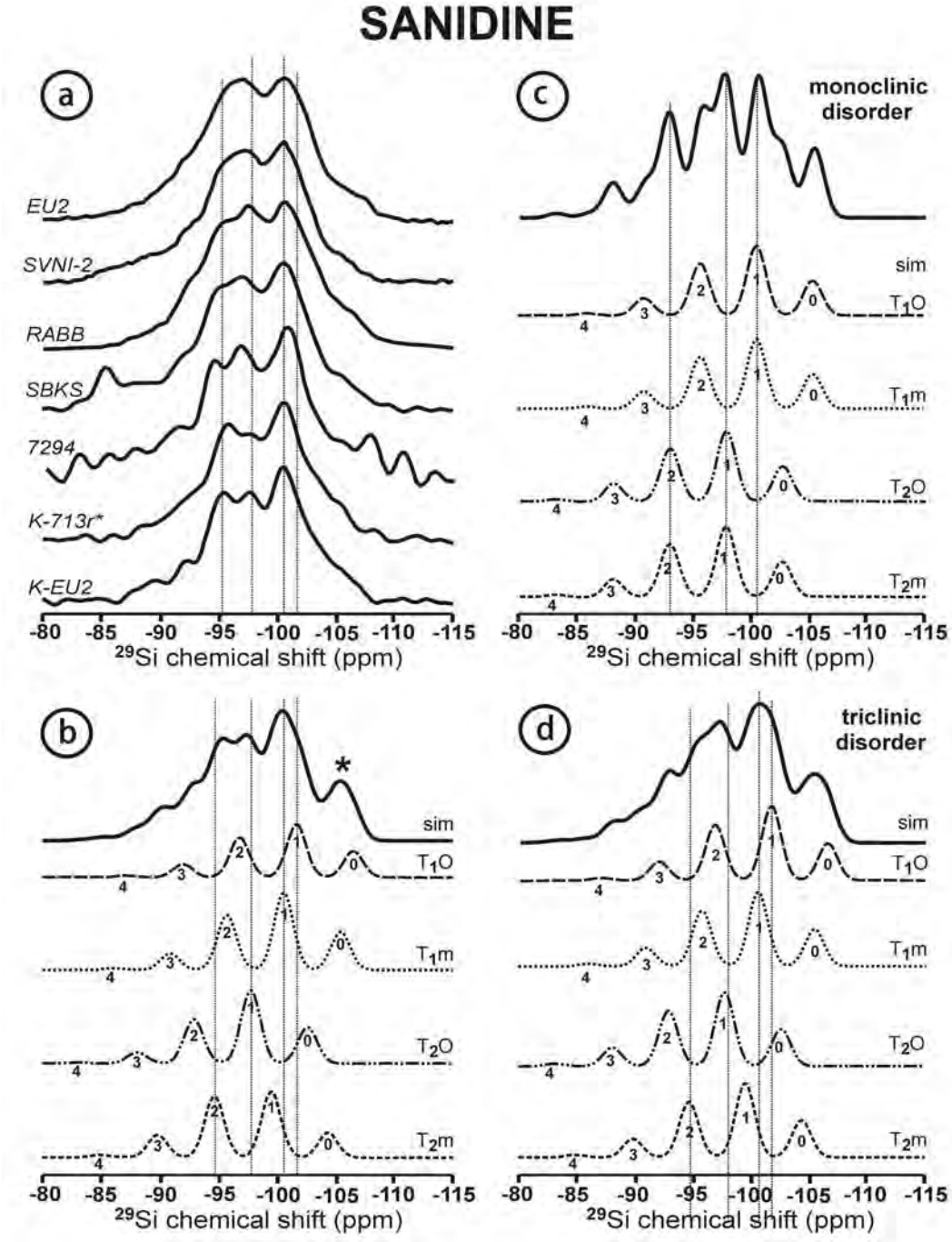
SANIDINE
a
EU2
SVNI-2
RABB
SBKS
7294
K-713r*
K-EU2
-80 -85 -90 -95 -100 -105 -110 -115
29Si chemical shift (ppm)
c
monoclinic disorder
sim
T1O
T1m
T2O
T2m
b
*
d
triclinic disorder

1360

Figure 5

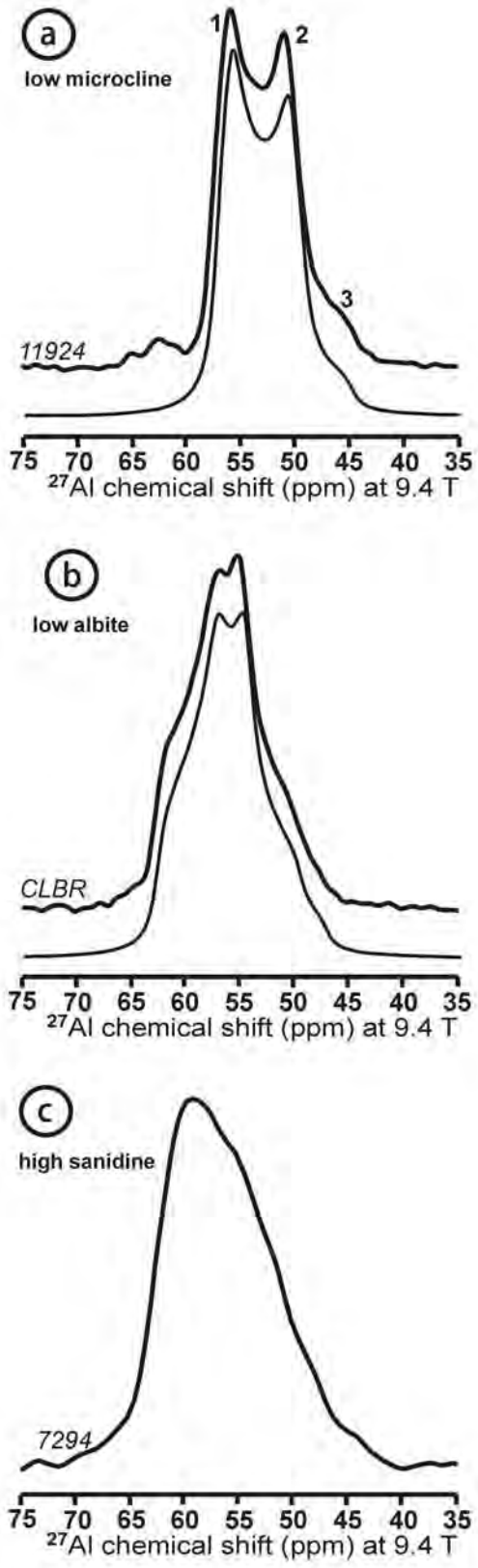

1361

Figure 6

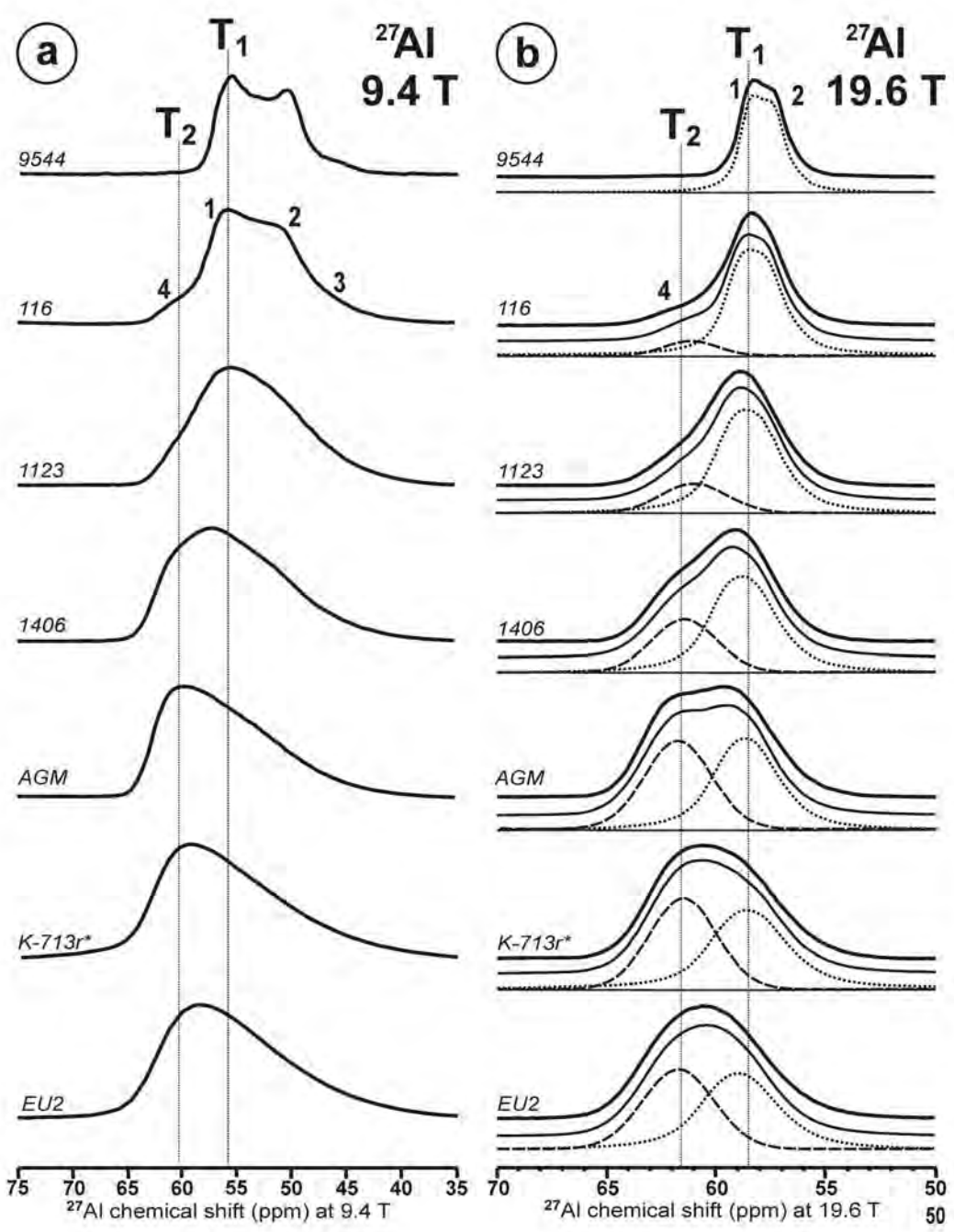
a
T1
T2
27Al
9.4 T
9544
116
1123
1406
AGM
K-713r*
EU2
1
2
3
4
75 70 65 60 55 50 45 40 35
27Al chemical shift (ppm) at 9.4 T
b
T1
T2
27Al
19.6 T
70 65 60 55 50
27Al chemical shift (ppm) at 19.6 T
50

Figure 7

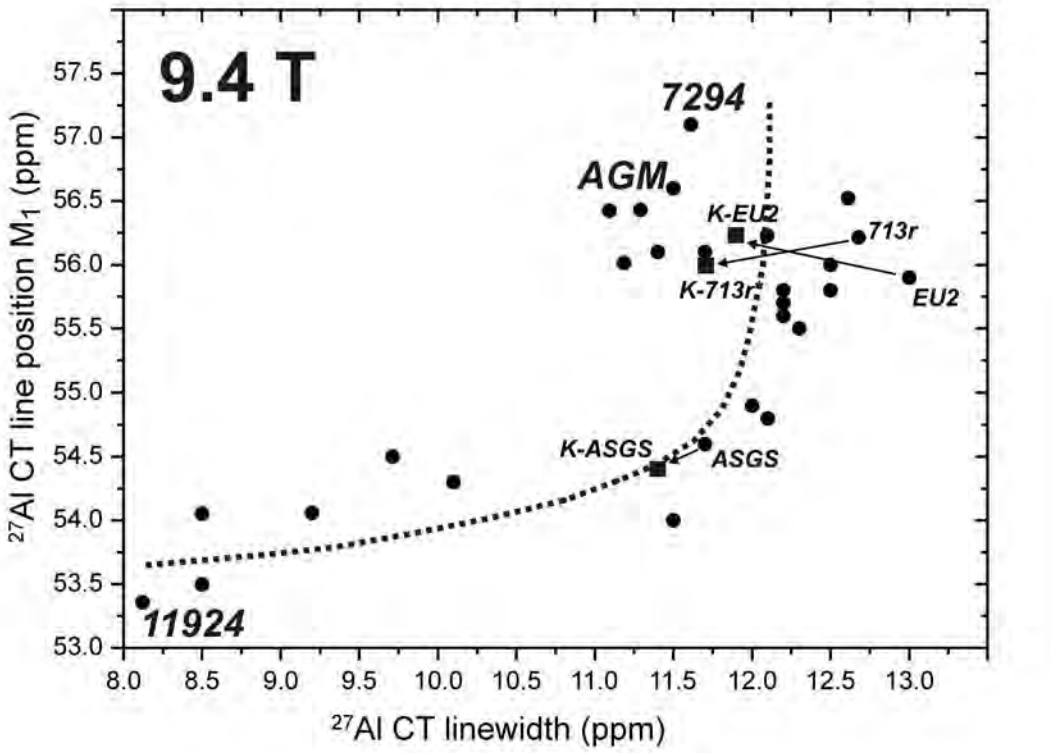
9.4 T
7294
AGM
K-EU2
713r
K-713r
EU2
K-ASGS
ASGS
11924
^{27}Al CT line position M_1 (ppm)
^{27}Al CT linewidth (ppm)
57.5
57.0
56.5
56.0
55.5
55.0
54.5
54.0
53.5
53.0
8.0
8.5
9.0
9.5
10.0
10.5
11.0
11.5
12.0
12.5
13.0

Figure 8

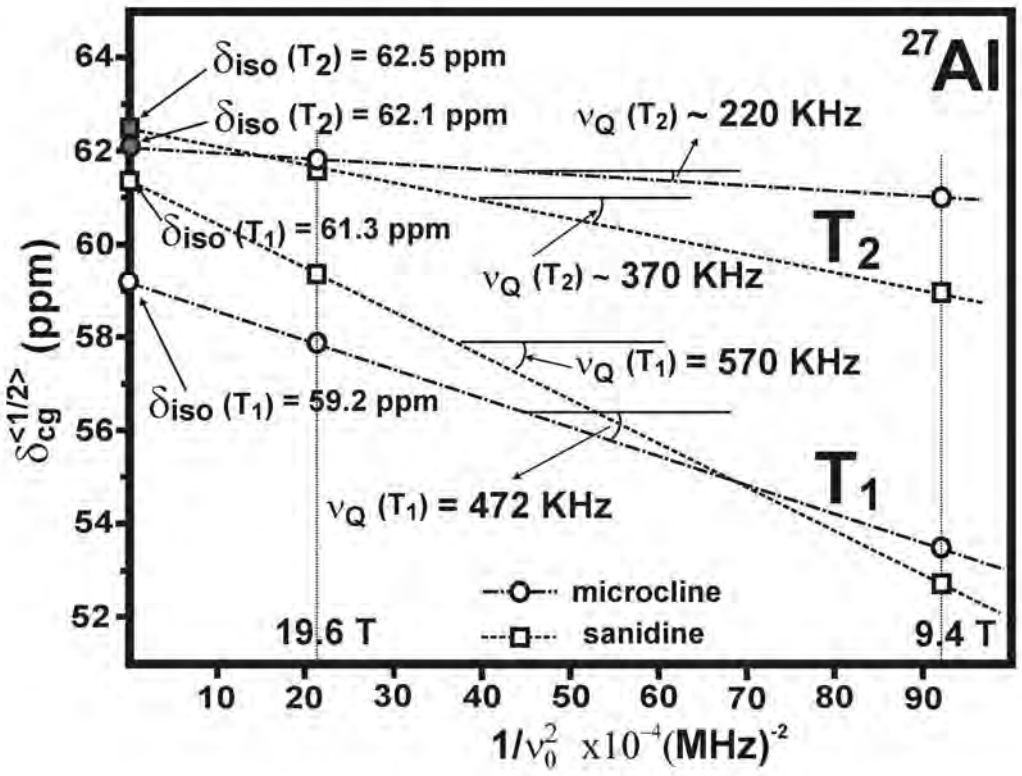
^{27}Al
δ_{iso} (T_2) = 62.5 ppm
δ_{iso} (T_2) = 62.1 ppm
ν_Q (T_2) ~ 220 KHz
δ_{iso} (T_1) = 61.3 ppm
ν_Q (T_2) ~ 370 KHz
T_2
ν_Q (T_1) = 570 KHz
δ_{iso} (T_1) = 59.2 ppm
T_1
ν_Q (T_1) = 472 KHz
microcline
sanidine
19.6 T
9.4 T
$\delta_{cg}^{<1/2>}$ (ppm)
64
62
60
58
56
54
52
10
20
30
40
50
60
70
80
90
$1/\nu_0^2$ x10^{-4}(MHz)$^{-2}$

Figure 9

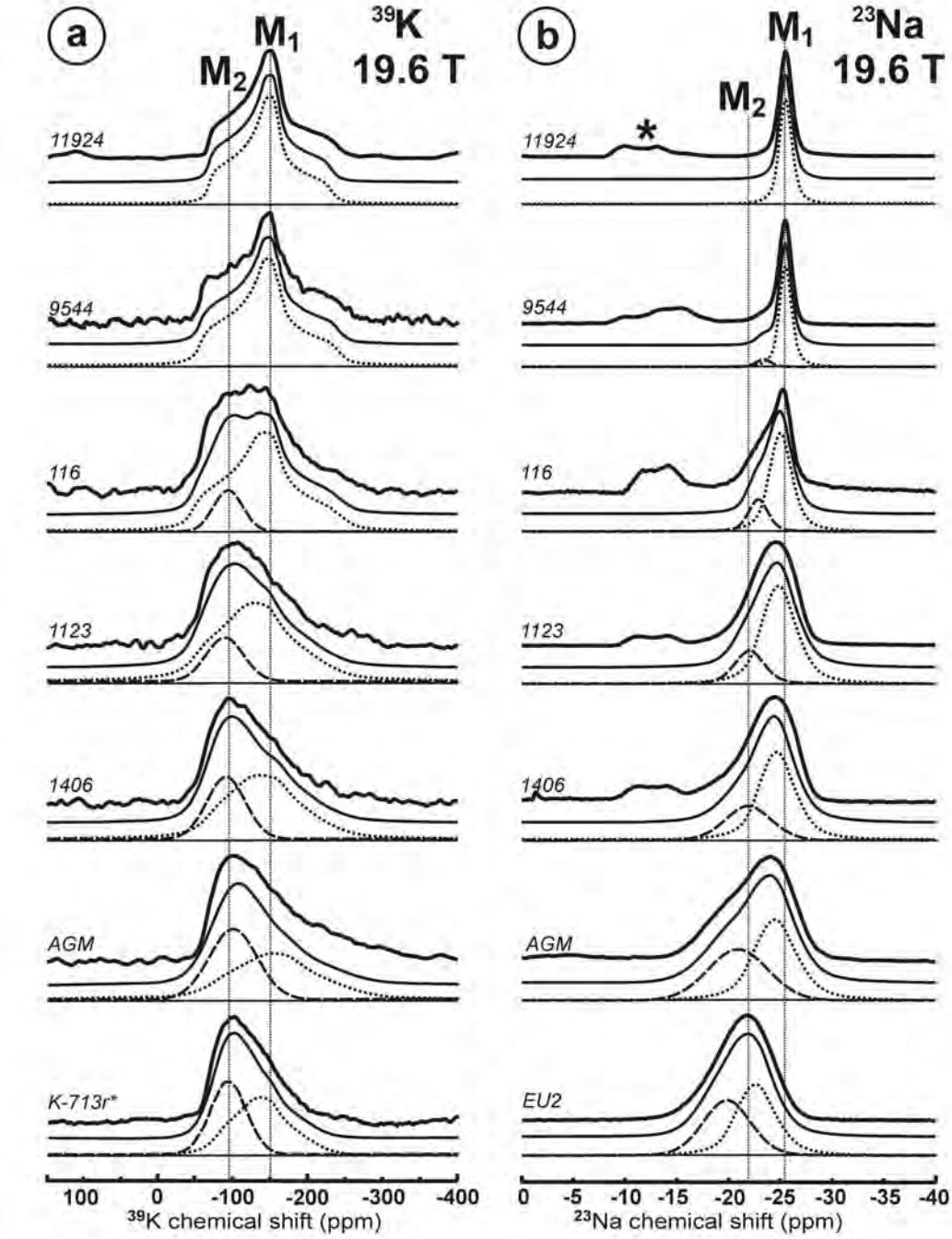
a
M1
M2
39K
19.6 T
11924
9544
116
1123
1406
AGM
K-713r*
100 0 -100 -200 -300 -400
39K chemical shift (ppm)
b
M1
M2
23Na
19.6 T
*
11924
9544
116
1123
1406
AGM
EU2
0 -5 -10 -15 -20 -25 -30 -35 -40
23Na chemical shift (ppm)

Figure 10

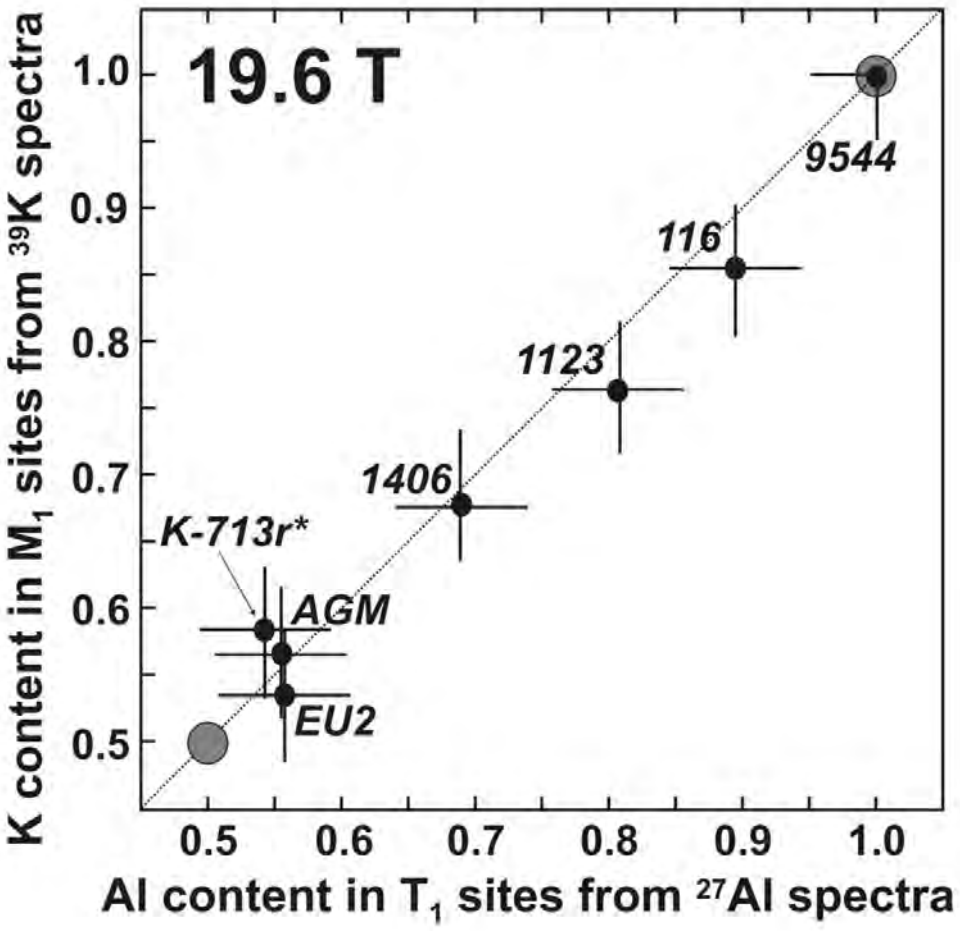
19.6 T
9544
116
1123
1406
K-713r*
AGM
EU2
1.0
0.9
0.8
0.7
0.6
0.5
0.5
0.6
0.7
0.8
0.9
1.0
K content in M1 sites from 39K spectra
Al content in T1 sites from 27Al spectra

Figure 11

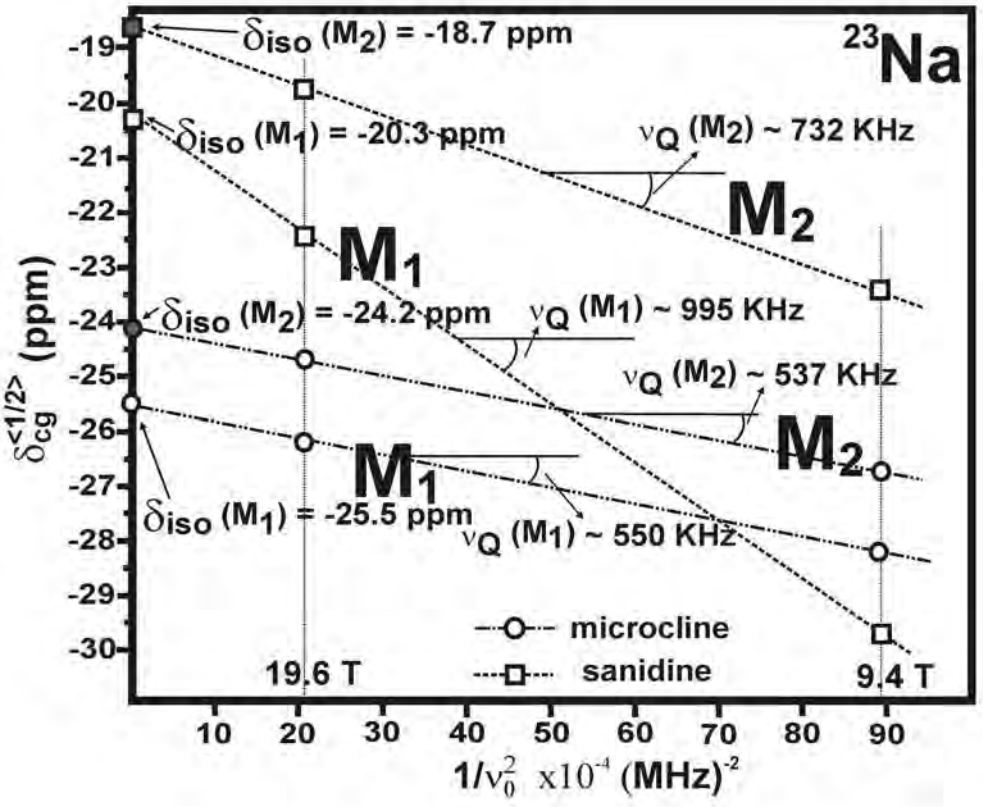
δiso (M2) = -18.7 ppm
23Na
δiso (M1) = -20.3 ppm
νQ (M2) ~ 732 KHz
M2
M1
δiso (M2) = -24.2 ppm
νQ (M1) ~ 995 KHz
νQ (M2) ~ 537 KHz
M2
M1
δiso (M1) = -25.5 ppm
νQ (M1) ~ 550 KHz
microcline
sanidine
19.6 T
9.4 T
δcg<1/2> (ppm)
1/ν0² x10⁻⁴ (MHz)⁻²

1474

Figure 12

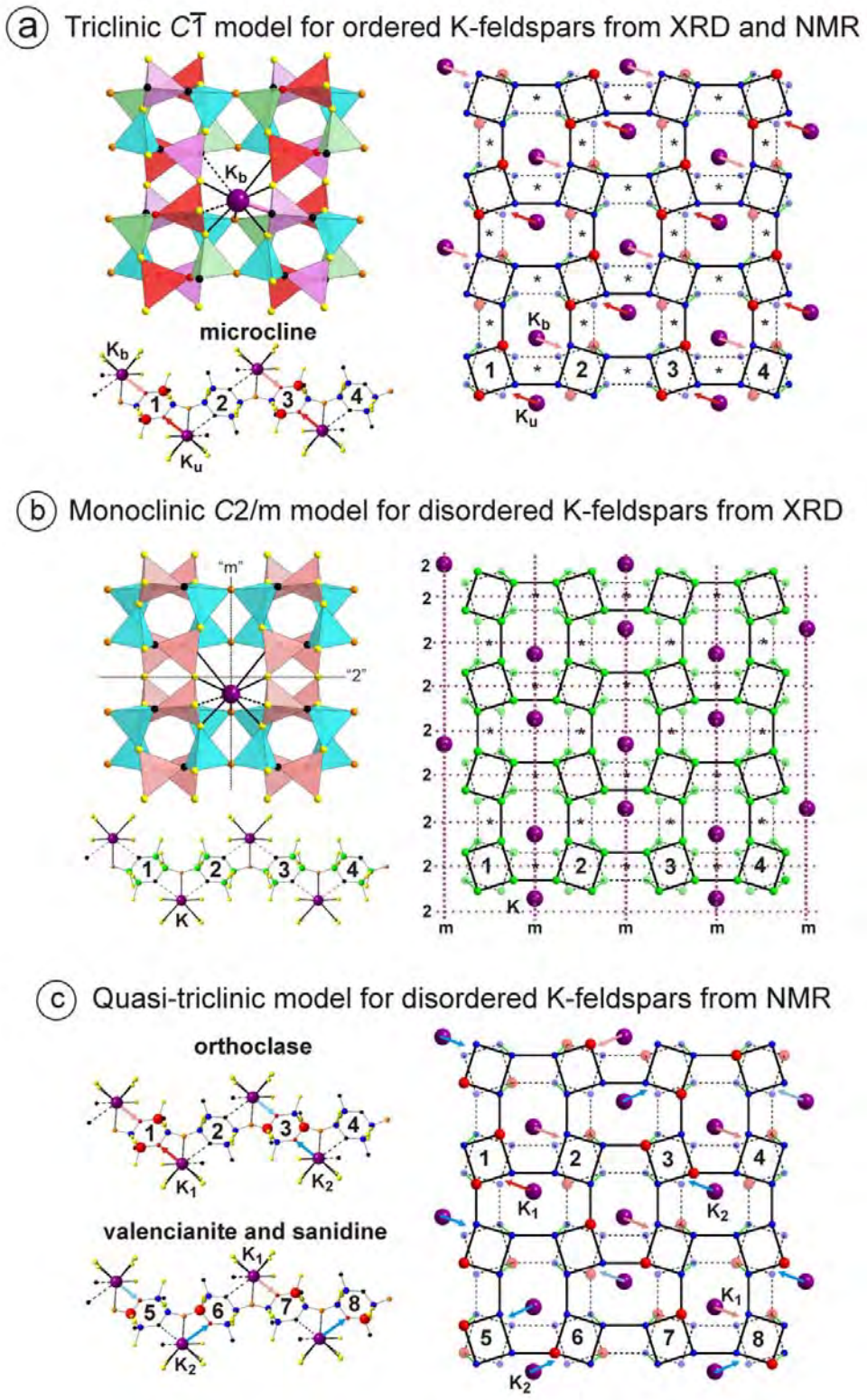

1475
1476
1477
1478

Supporting information online

Table 5

Peak intensities of the specific simulations of the ^{29}Si MAS NMR spectra

Specimens	*9544*	*176*	*116*	*FB4*	*K-ASGS*	*1406*	*AGM*		*K-EU2*
							sim1	sim2	
T_1O (0Si, 4Al)	0.00	0.06	0.11	0.12	0.12	0.10	0.25	-	0.23
T_1O (1Si, 3Al)	0.00	0.44	0.92	0.99	1.36	1.04	1.98	-	1.95
T_1O (2Si, 2Al)	0.00	1.20	2.52	2.78	4.35	3.75	5.94	-	5.98
T_1O (3Si, 1Al)	0.00	1.39	2.75	3.33	3.40	5.63	7.92	20.00	7.97
T_1O (4Si, 0Al)	0.00	0.58	1.03	1.45	0.77	2.81	3.96	-	3.89
T_1m (0Si, 4Al)	0.00	0.00	0.01	0.03	0.01	0.11	0.21	-	0.27
T_1m (1Si, 3Al)	0.00	0.12	0.45	0.71	0.55	1.70	2.09	-	2.49
T_1m (2Si, 2Al)	0.00	3.13	5.46	6.32	6.44	8.32	7.51	-	8.26
T_1m (3Si, 1Al)	33.33	26.71	21.35	19.47	18.77	14.51	11.27	26.66	11.62
T_1m (4Si, 0Al)	0.00	2.38	4.40	4.81	5.91	5.38	5.63	-	5.72
T_2O (0Si, 4Al)	0.00	0.00	0.01	0.01	0.01	0.04	0.21	-	0.14
T_2O (1Si, 3Al)	0.00	0.12	0.37	0.46	0.55	0.83	2.09	-	1.66
T_2O (2Si, 2Al)	0.00	3.13	5.11	5.36	6.43	5.95	7.31	-	6.63
T_2O (3Si, 1Al)	33.33	26.71	21.62	20.13	18.77	15.32	11.27	26.66	11.00
T_2O (4Si, 0Al)	0.00	2.38	4.22	4.35	5.91	4.47	5.64	-	5.48
T_2m (0Si, 4Al)	0.00	0.03	0.09	0.14	0.08	0.33	0.42	-	0.39
T_2m (1Si, 3Al)	0.00	1.70	2.67	3.23	2.42	4.12	3.34	-	3.34
T_2m (2Si, 2Al)	33.33	26.30	20.81	18.49	18.63	13.09	9.18	26.66	9.23
T_2m (3Si, 1Al)	0.00	3.52	5.71	7.10	5.18	10.17	10.02	-	10.01
T_2m (4Si, 0Al)	0.00	0.12	0.40	0.71	0.37	2.31	3.76	-	3.73

Peak intensities in % are calculated assuming a constant Si/Al ratio of 3.0 and Loewenstein's Al-O-Al avoidance rule, after Xiao et al. (1995). The chemical shifts produced by replacement of Si by Al, to calculate different possible Si Q^4 (nAl) n = 0, 1, 2, 3, 4, was assumed ± 4.85 ppm in all cases. The δ_x values are in ppm.

Table 6. Simulation of the ^{29}Si NMR spectra of the order-disorder models

Alternative models	*Two-step Orthoclase* Fig. 2c	*One-step Orthoclase* Fig.2d	*Triclinic High sanidine* Fig. 4c	*Monoclinic High sanidine* Fig. 4d
Linewidth	1.10	1.10	1.35	1.35
t_1O	0.40	0.70	0.25	
t_1m	0.40	0.10	0.25	
t_2O	0.10	0.10	0.25	
t_2m	0.10	0.10	0.25	0.25
δT_1O (3Si,1Al)	-100.8	-101.7	-101.7	-100.6
δT_1m (3Si,1Al)	-100.8	-100.8	-100.6	-100.6
δT_2O (3Si,1Al)	-96.5	-97.8	-97.8	-97.8
δT_2m (2Si,2Al)	-91.7	-94.7	-94.7	-93.0
T_1O (0Si, 4Al)	0.06	0.12	0.31	
T_1O (1Si, 3Al)	0.97	0.99	2,47	
T_1O (2Si, 2Al)	5.15	2.96	7.41	
T_1O (3Si, 1Al)	10.14	3.95	9.88	
T_1O (4Si, 0Al)	3.90	1.98	4.94	
T_1m (0Si, 4Al)	0.06	0.03	0.31	
T_1m (1Si, 3Al)	0.97	0.78	2.47	
T_1m (2Si, 2Al)	5.15	6.37	7.41	
T_1m (3Si, 1Al)	10.14	18.15	9.88	
T_1m (4Si, 0Al)	3.90	4.68	4.94	
T_2O (0Si, 4Al)	0.30	0.03	0.31	
T_2O (1Si, 3Al)	3.48	0.78	2.47	
T_2O (2Si, 2Al)	9.15	6.31	7.41	
T_2O (3Si, 1Al)	11.67	18.15	9.88	
T_2O (4Si, 0Al)	4.62	4.68	4.94	
T_2m (0Si, 4Al)	0.30	0.22	0.31	
T_2m (1Si, 3Al)	3.48	3.71	2.47	
T_2m (2Si, 2Al)	10.26	16.42	7.41	
T_2m (3Si, 1Al)	11.67	8.49	9.88	
T_2m (4Si, 0Al)	4.62	1.17	4.94	

The letter "t" lowercase is used for the Al content in the tetrahedral sites, which are named with "T" uppercase. Peak intensities in % are calculated assuming a constant Si/Al ratio of 3.0 and Loewenstein's Al-O-Al avoidance rule, after Xiao et al. (1995). The chemical shifts produced by replacement of Si by Al, to calculate different possible Si Q^4 (nAl) n = 0, 1, 2, 3, 4, was of ± 4.85 ppm in all cases. The δ_x values are in ppm.

1527
1528

MICROCLINE

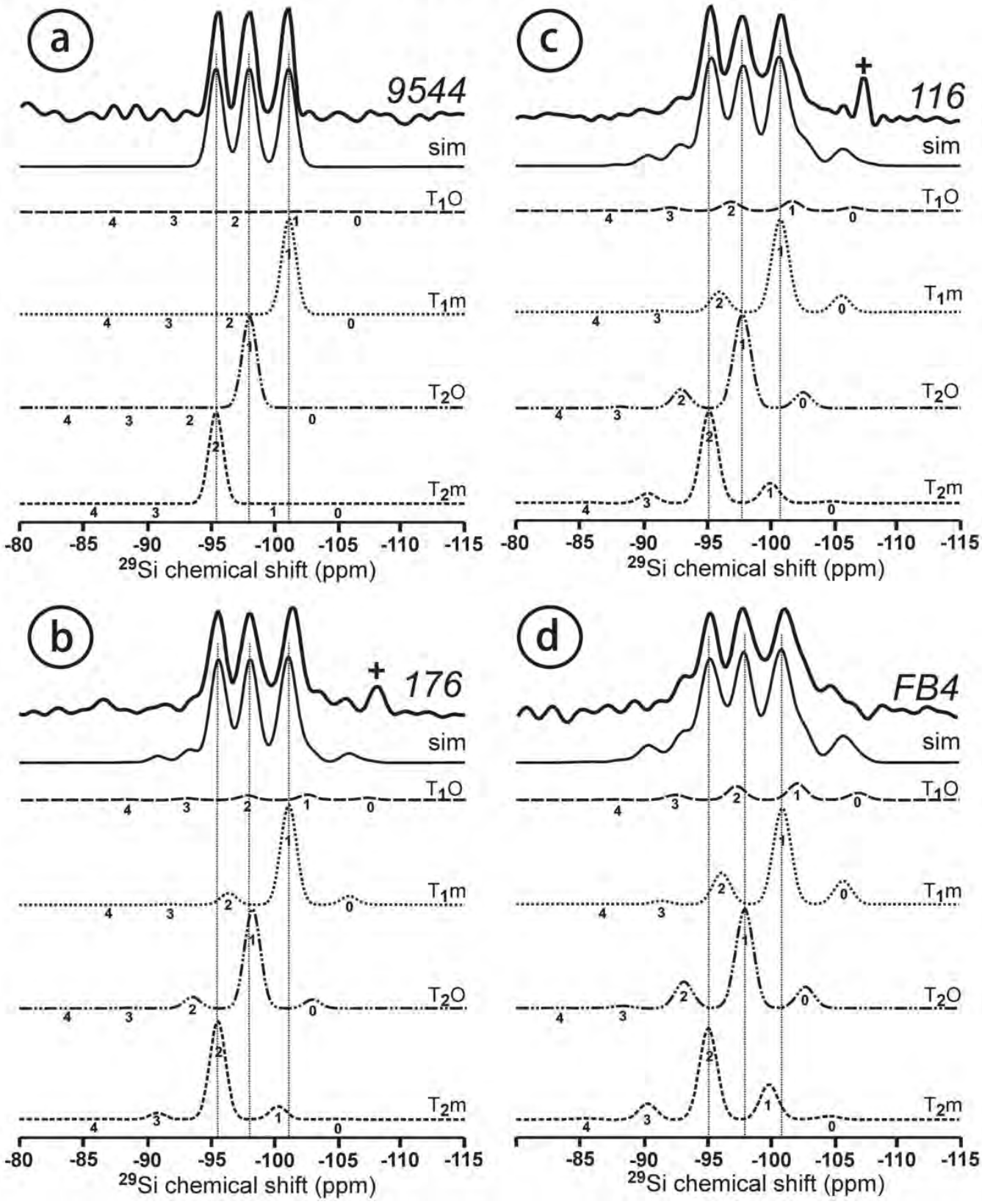
a
9544
sim
T1O
T1m
T2O
T2m
-80 -85 -90 -95 -100 -105 -110 -115
29Si chemical shift (ppm)
c
116
sim
T1O
T1m
T2O
T2m
-80 -85 -90 -95 -100 -105 -110 -115
29Si chemical shift (ppm)
b
176
sim
T1O
T1m
T2O
T2m
-80 -85 -90 -95 -100 -105 -110 -115
29Si chemical shift (ppm)
d
FB4
sim
T1O
T1m
T2O
T2m
-85 -90 -95 -100 -105 -110 -115
29Si chemical shift (ppm)

ORTHOCLASE

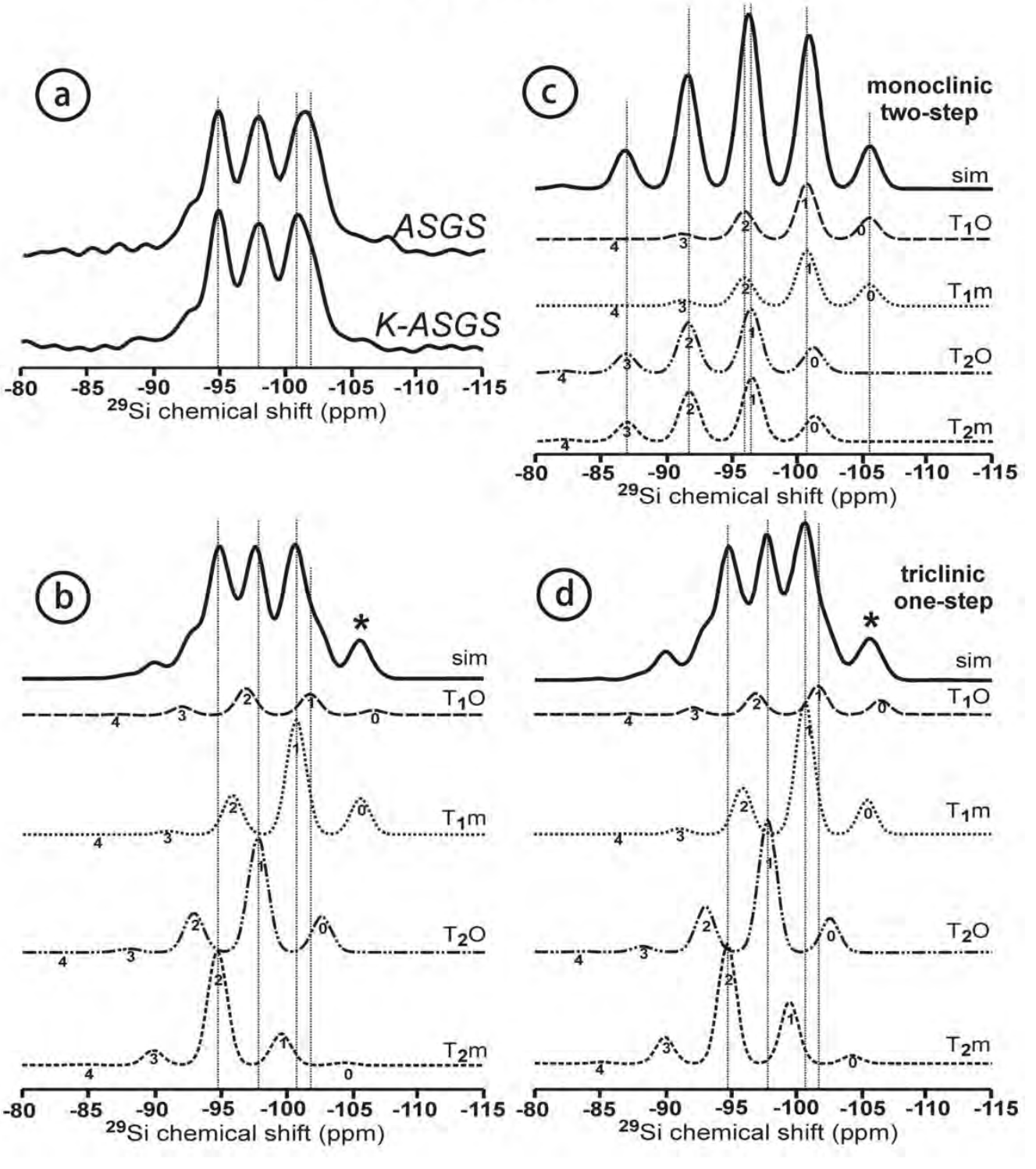
a
ASGS
K-ASGS
-80 -85 -90 -95 -100 -105 -110 -115
29Si chemical shift (ppm)
c
monoclinic
two-step
sim
T1O
T1m
T2O
T2m
-80 -85 -90 -95 -100 -105 -110 -115
29Si chemical shift (ppm)
b
*
sim
T1O
T1m
T2O
T2m
-80 -85 -90 -95 -100 -105 -110 -115
29Si chemical shift (ppm)
d
triclinic
one-step
*
sim
T1O
T1m
T2O
T2m
-80 -85 -90 -95 -100 -105 -110 -115
29Si chemical shift (ppm)

VALENCIANITE

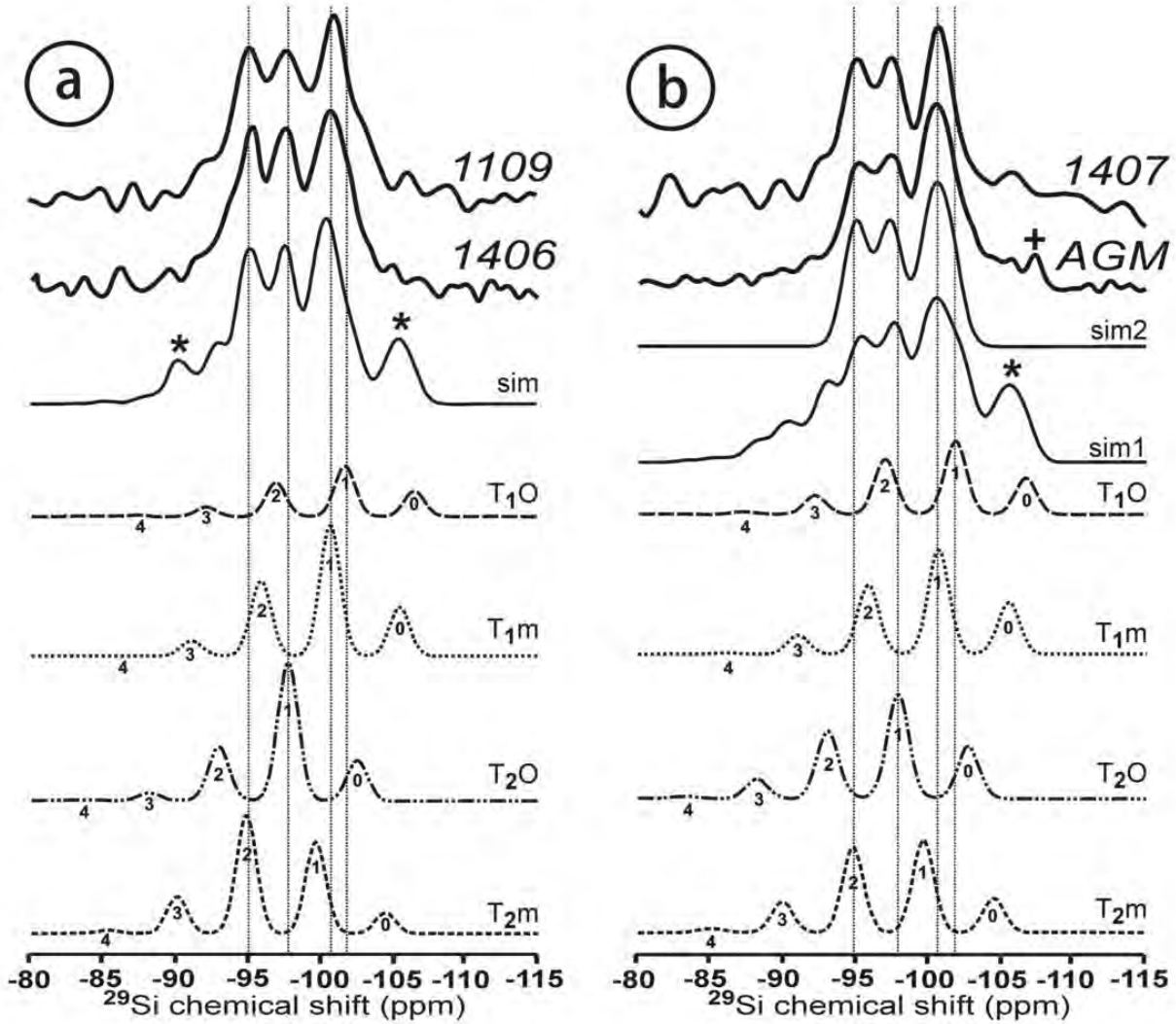

SANIDINE

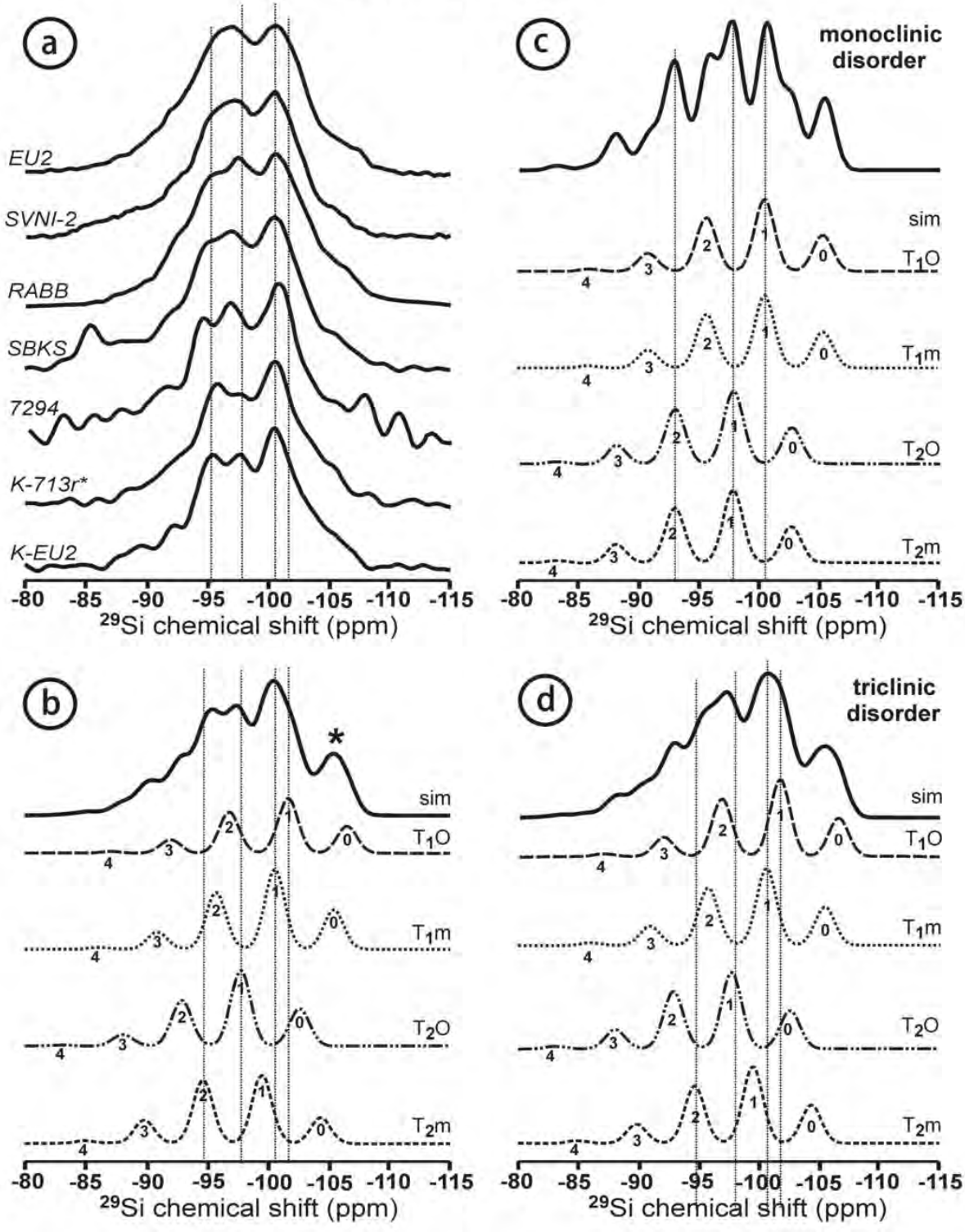
a
EU2
SVNI-2
RABB
SBKS
7294
K-713r*
K-EU2
-80 -85 -90 -95 -100 -105 -110 -115
29Si chemical shift (ppm)
c
monoclinic disorder
sim
T1O
T1m
T2O
T2m
b
*
d
triclinic disorder

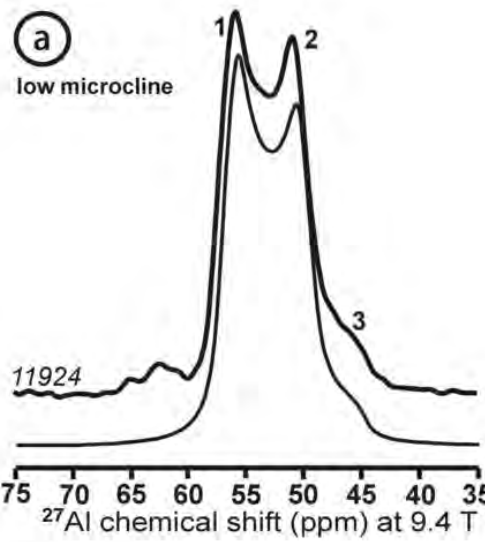
a
low microcline
1
2
3
11924
75 70 65 60 55 50 45 40 35
27Al chemical shift (ppm) at 9.4 T

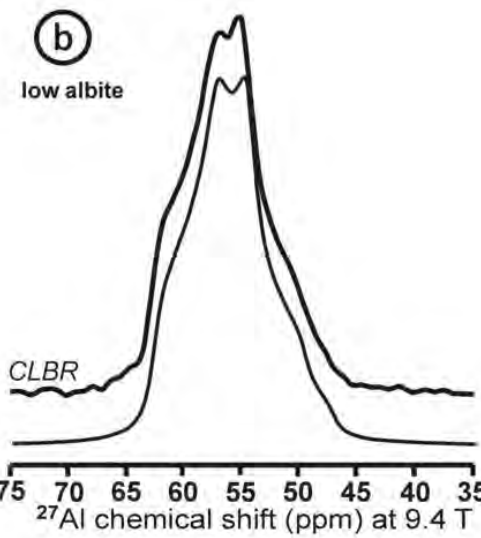
b
low albite
CLBR
75 70 65 60 55 50 45 40 35
27Al chemical shift (ppm) at 9.4 T

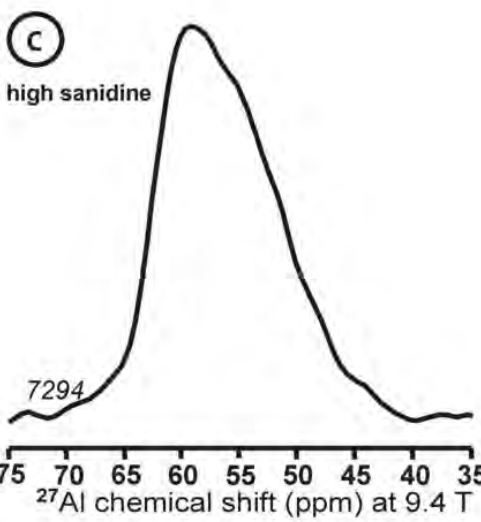
c
high sanidine
7294
75 70 65 60 55 50 45 40 35
27Al chemical shift (ppm) at 9.4 T

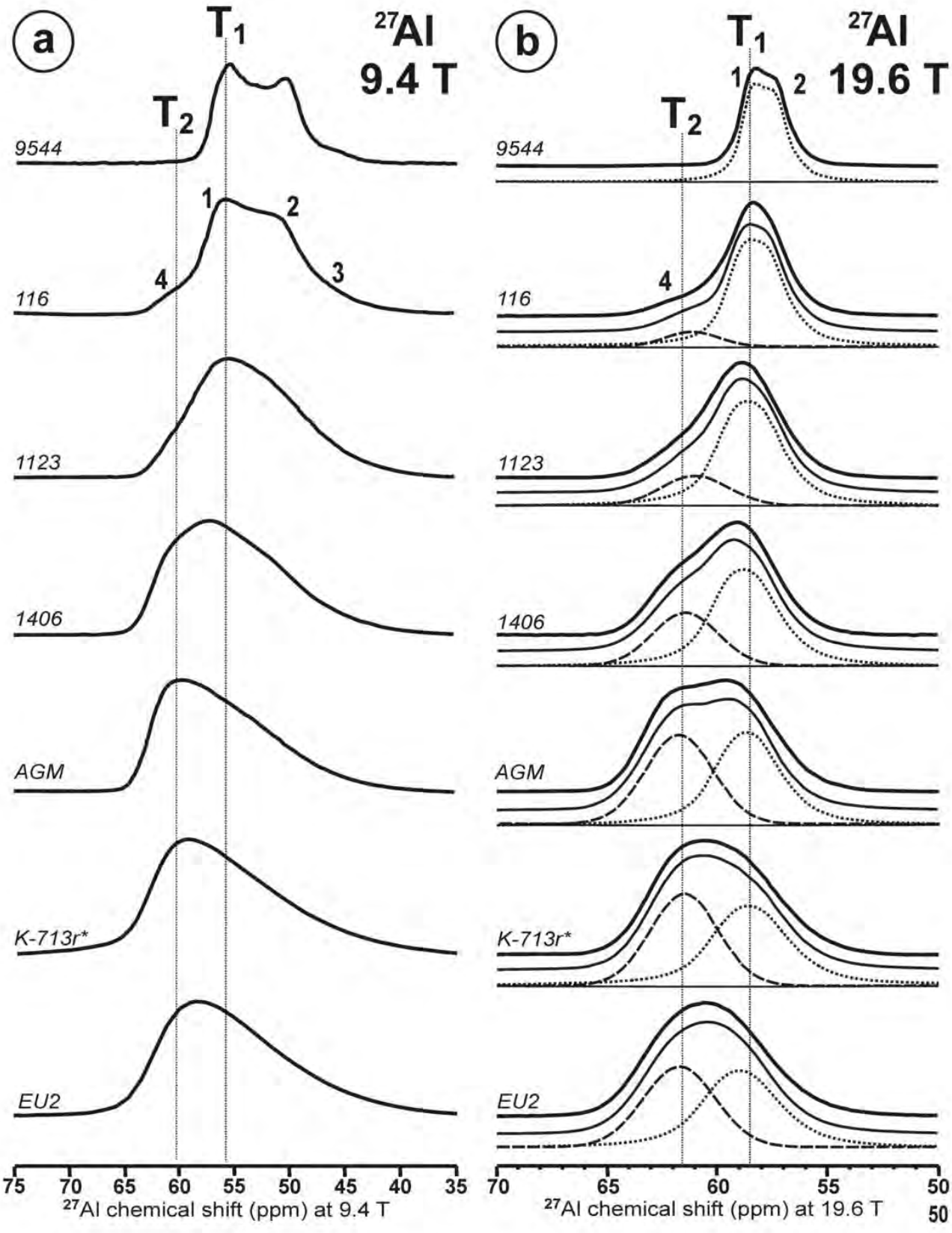
a
T1
27Al
9.4 T
T2
9544
1
2
116
4
3
1123
1406
AGM
K-713r*
EU2
75 70 65 60 55 50 45 40 35
27Al chemical shift (ppm) at 9.4 T
b
T1
27Al
19.6 T
1
2
T2
9544
116
4
1123
1406
AGM
K-713r*
EU2
70 65 60 55 50
27Al chemical shift (ppm) at 19.6 T

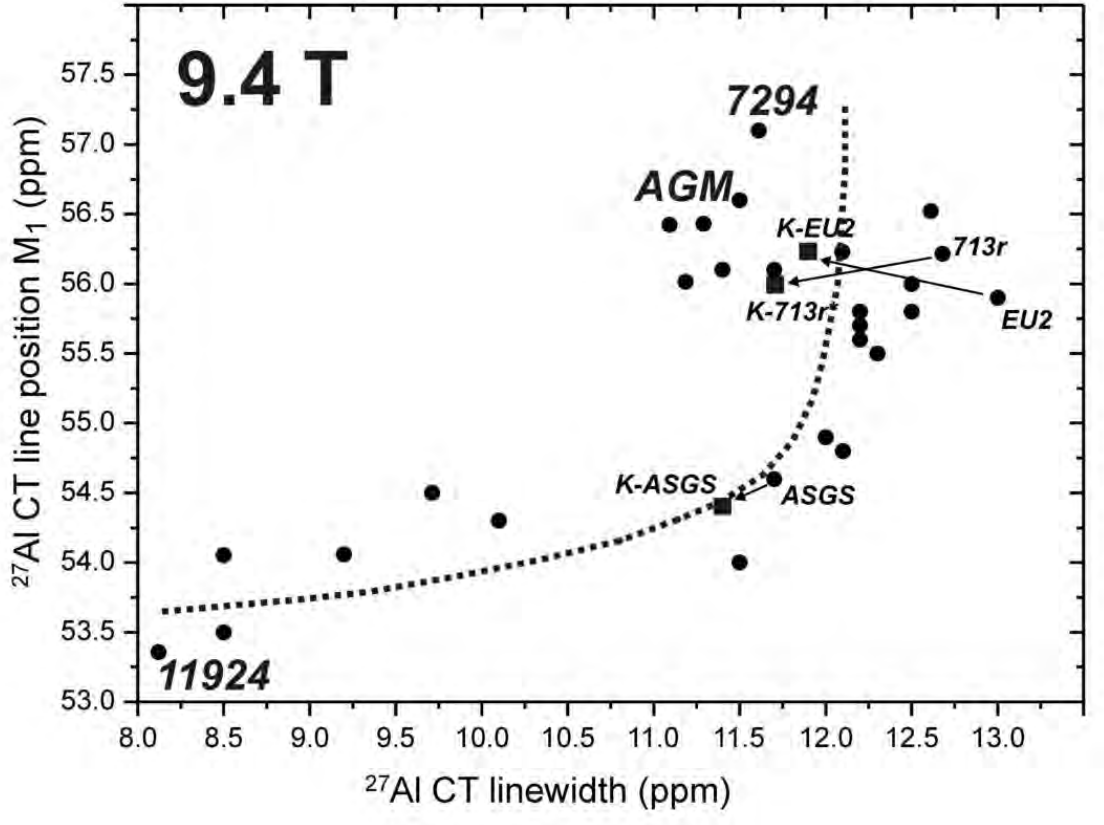
9.4 T
7294
AGM
K-EU2
713r
K-713r
EU2
K-ASGS
ASGS
11924
57.5
57.0
56.5
56.0
55.5
55.0
54.5
54.0
53.5
53.0
8.0
8.5
9.0
9.5
10.0
10.5
11.0
11.5
12.0
12.5
13.0
27Al CT line position M1 (ppm)
27Al CT linewidth (ppm)

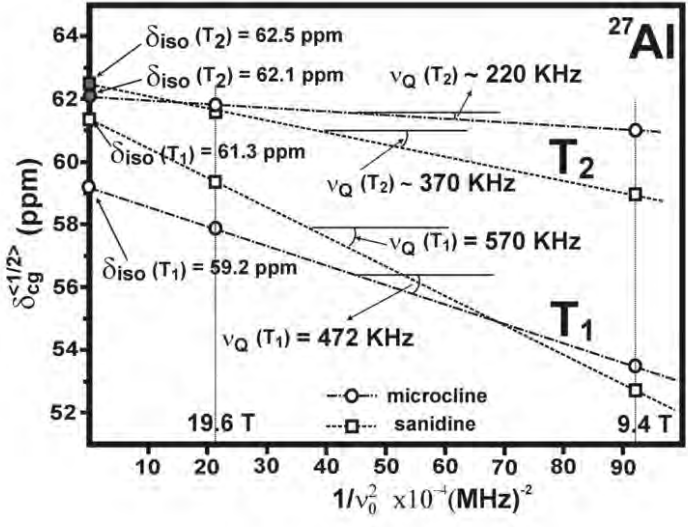
^{27}Al
δ_{iso} (T_2) = 62.5 ppm
δ_{iso} (T_2) = 62.1 ppm
ν_Q (T_2) ~ 220 KHz
δ_{iso} (T_1) = 61.3 ppm
ν_Q (T_2) ~ 370 KHz
T_2
ν_Q (T_1) = 570 KHz
δ_{iso} (T_1) = 59.2 ppm
T_1
ν_Q (T_1) = 472 KHz
microcline
sanidine
19.6 T
9.4 T
$\delta_{cg}^{<1/2>}$ (ppm)
$1/\nu_0^2$ x10^{-4}(MHz)$^{-2}$
64
62
60
58
56
54
52
10
20
30
40
50
60
70
80
90

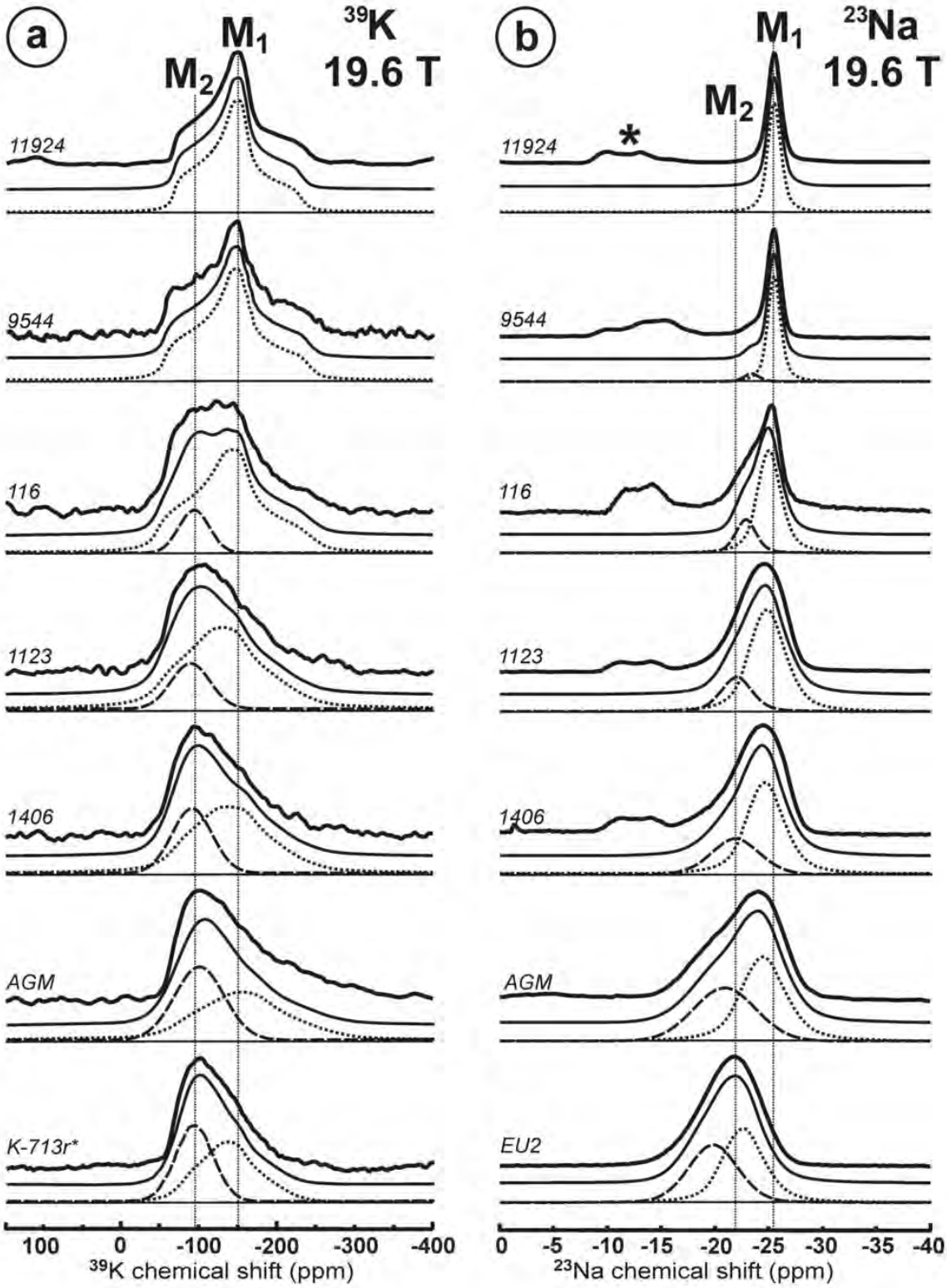
a
M1
M2
39K
19.6 T
11924
9544
116
1123
1406
AGM
K-713r*
100
0
-100
-200
-300
-400
39K chemical shift (ppm)
b
M1
M2
23Na
19.6 T
*
11924
9544
116
1123
1406
AGM
EU2
0
-5
-10
-15
-20
-25
-30
-35
-40
23Na chemical shift (ppm)

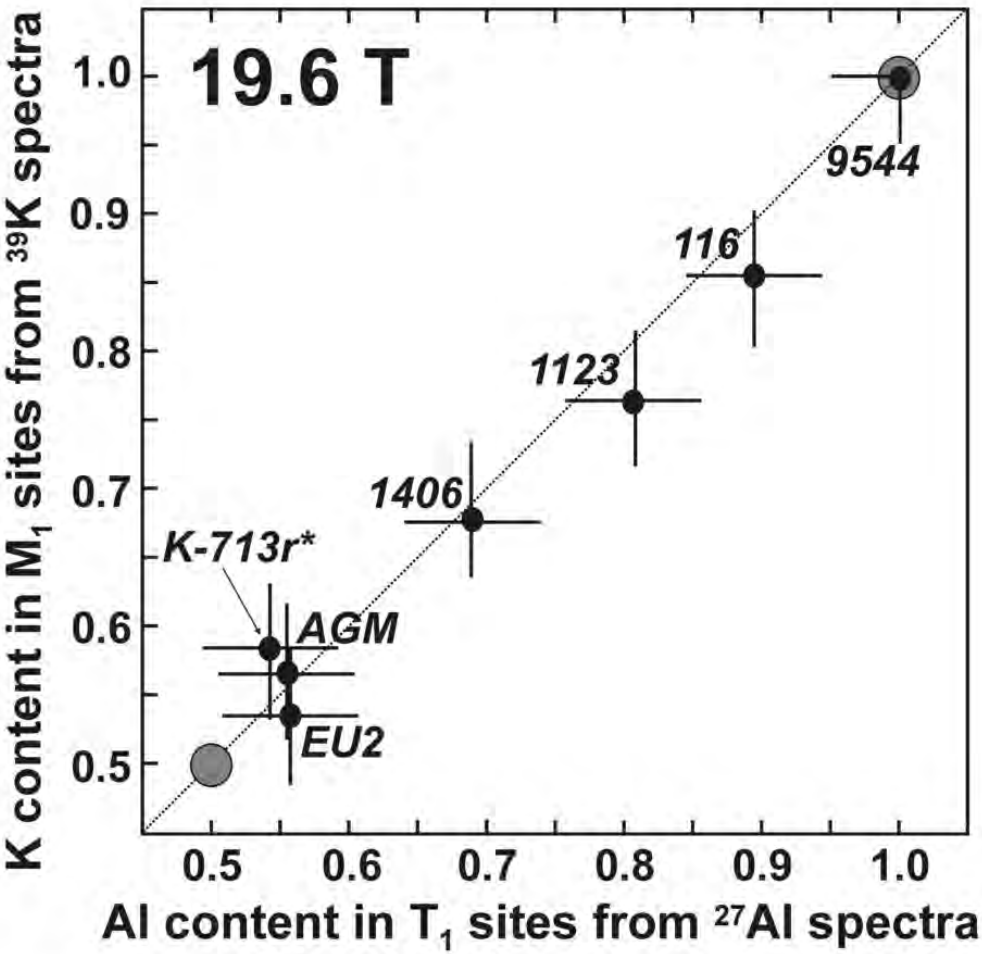
19.6 T
9544
116
1123
1406
K-713r*
AGM
EU2
1.0
0.9
0.8
0.7
0.6
0.5
0.5
0.6
0.7
0.8
0.9
1.0
K content in M1 sites from 39K spectra
Al content in T1 sites from 27Al spectra

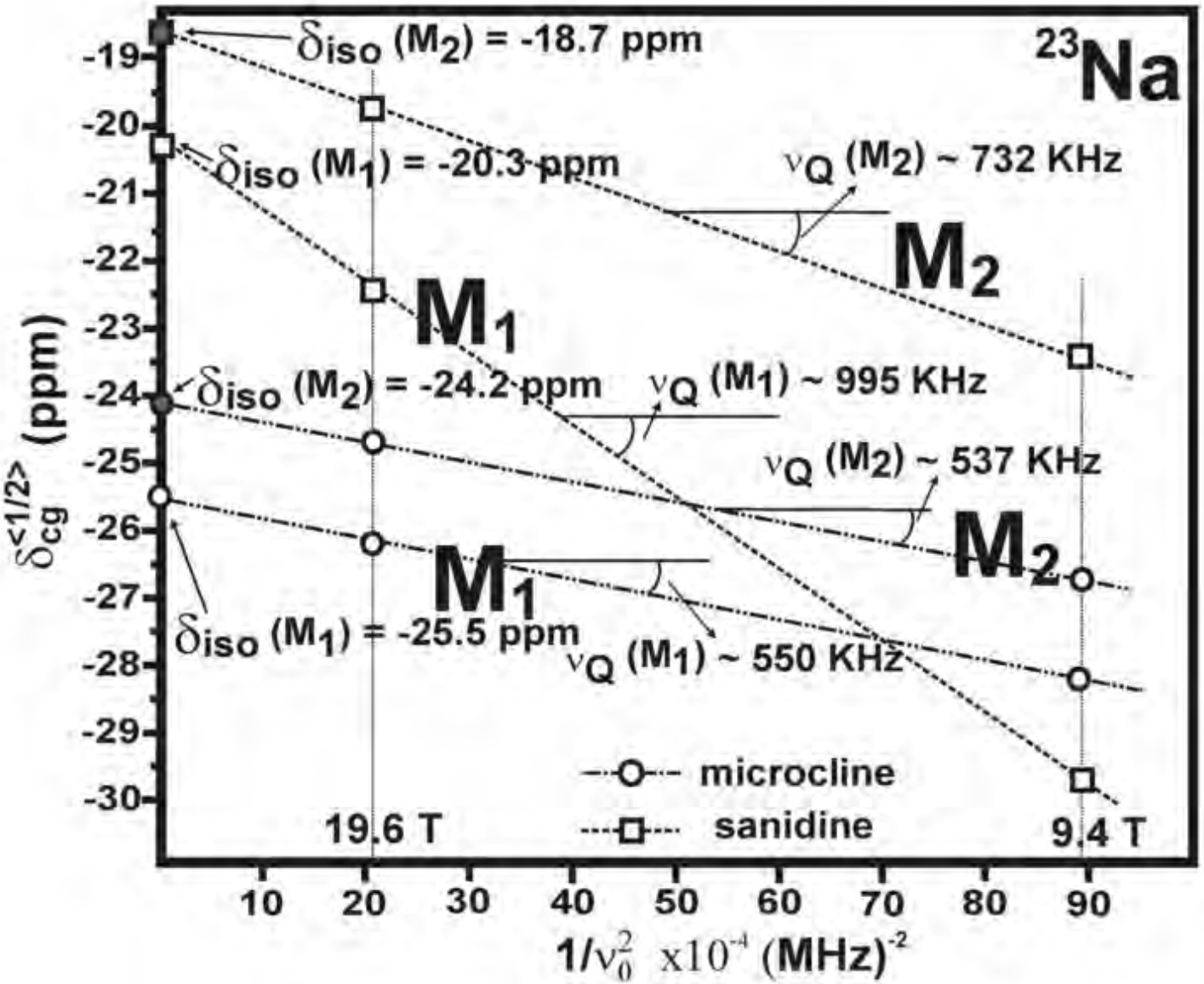
^{23}Na
δ_{iso} (M_2) = -18.7 ppm
δ_{iso} (M_1) = -20.3 ppm
ν_Q (M_2) ~ 732 KHz
M_2
M_1
δ_{iso} (M_2) = -24.2 ppm
ν_Q (M_1) ~ 995 KHz
ν_Q (M_2) ~ 537 KHz
M_2
M_1
δ_{iso} (M_1) = -25.5 ppm
ν_Q (M_1) ~ 550 KHz
microcline
sanidine
19.6 T
9.4 T
$\delta_{cg}^{<1/2>}$ (ppm)
-19
-20
-21
-22
-23
-24
-25
-26
-27
-28
-29
-30
10
20
30
40
50
60
70
80
90
$1/\nu_0^2$ x10^{-4} (MHz)$^{-2}$

ⓐ Triclinic $C\bar{1}$ model for ordered K-feldspars from XRD and NMR

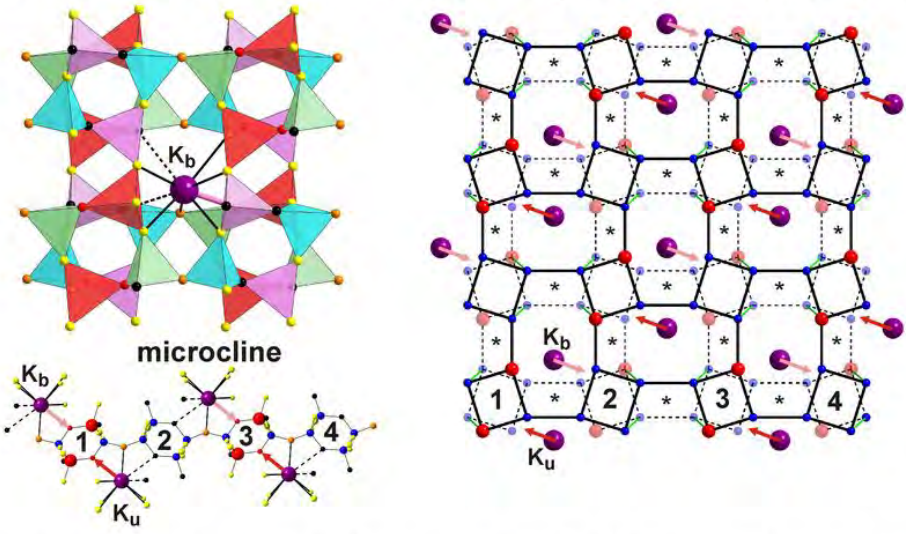

ⓑ Monoclinic *C*2/m model for disordered K-feldspars from XRD

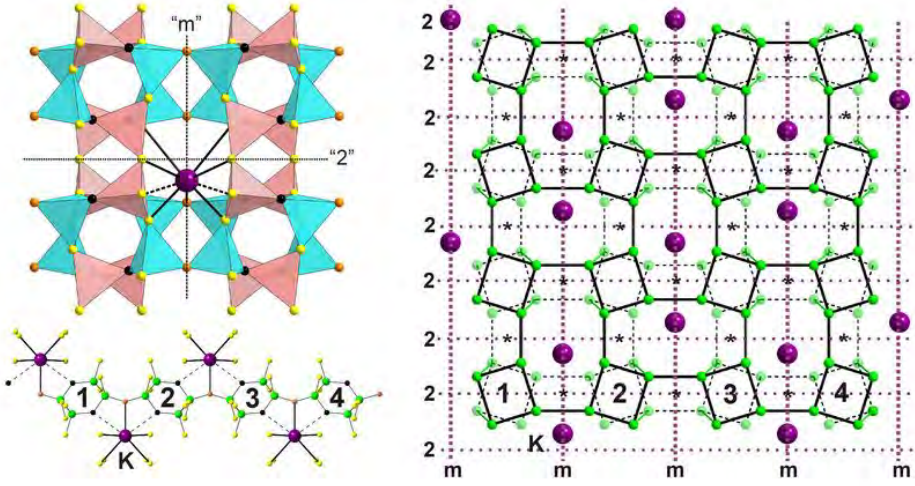

ⓒ Quasi-triclinic model for disordered K-feldspars from NMR